Investigating microstructure evolution in block copolymer membranes

Anthony J. Cooper,[*,†] Douglas J. Grzetic,[*,¶] Kris T. Delaney,[*,‡] and Glenn H. Fredrickson[*,‡]

†*Department of Physics, University of California, Santa Barbara, California 93106, USA*

‡*Materials Research Laboratory, University of California, Santa Barbara, California 93106, USA*

¶*Schrödinger Inc, 101 SW Main St Portland OR 97204, USA*

§*Departments of Chemical Engineering and Materials, University of California, Santa Barbara, California 93106, USA*

E-mail: acooper@ucsb.edu; dgrzetic@ucsb.edu; kdelaney@mrl.ucsb.edu; ghf@ucsb.edu

Abstract

Block copolymer self-assembly in conjunction with nonsolvent-induced phase separation (SNIPS) has been increasingly leveraged to fabricate integral-asymmetric membranes. The large number of formulation and processing parameters associated with SNIPS, however, has prevented the reliable construction of high performance membranes. In this study, we apply dynamical self-consistent field theory to model the SNIPS process and investigate the effect of various parameters on the membrane morphology: solvent selectivity, nonsolvent selectivity, initial film composition, and glass transition composition. We examine how solvent selectivity and concentration of polymer in the film impacts the structure of micelles that connect to form the membrane matrix. In particular, we find that preserving the order in the surface layer and forming a connection between the supporting and surface layer is nontrivial and sensitive to

each parameter studied. The effect of each parameter is discussed and suggestions are made for successfully fabricating viable block copolymer membranes.

1. Introduction

Factors such as population growth, increased urbanization, and climate change have led to a rise in water stressed regions around the globe.[1] As a result, efforts to innovate water desalination[2,3] and wastewater treatment processes[4] have been made to increase access to clean water. To this end, polymer-based membranes have seen widespread application and research due to their ability to separate out contaminants with high energy efficiency.[5,6]

With pores sizes on the order of $1-100$ nm, ultrafiltration (UF) membranes have seen extensive use in water treatment processes filtering out proteins, viruses, and other microbes.[7] UF membranes are typically fabricated using a method known as nonsolvent-induced phase separation (NIPS) in which a polymer solution is cast onto a substrate and immediately immersed into a nonsolvent bath, driving phase separation in the film resulting in a polymer-rich membrane matrix and a polymer-poor porous network.[8,9] The characteristic advantage of NIPS membranes, which are typically produced with homopolymers, is the asymmetric structure in which smaller, selective pores populate the surface while pore size increases as a function of film depth, enabling simultaneous high selectivity and water permeability.

While the asymmetric structure emerging from NIPS is ideal, NIPS membranes suffer from a broad pore size distribution at the surface, limiting its size selectivity.[10,11] A promising alternative is to use a block copolymer as the membrane material, leveraging its self-assembly properties to form an isoporous surface.[12–16] Successful block copolymer membranes generally present a cylindrical nanostructure at the surface, with cylinders oriented parallel to the axis of water flow, as well as the asymmetric structure in the support layer. Although debate exists,[14] it is generally thought that the cylindrical cores are composed of a hydrophilic, minority block encased in a matrix formed by a hydrophobic, glassy majority block.[13,16] It has

been reported that integral-asymmetric block copolymer membranes surpass the selectivity-permeability trade-off that plagues standard homopolymer NIPS membranes.[12]

Methods to fabricate block copolymer membranes are numerous, which can be either equilibrium or non-equilibrium in nature.[13] Owing to its ease of deployment on an industrial scale and constructing both the surface and bulk morphology within a continuous workflow, a method that employs block copolymer self-assembly in conjuction with NIPS (SNIPS) has gained significant attention since its first reported use by Peinemann *et al.*[17] This so-called SNIPS procedure is outlined by the following steps: (1) dissolve a block copolymer in one or more solvents, (2) evaporate the solvent(s) from the surface to produce a thin skin layer and induce block copolymer self-assembly, and (3) immerse the film in a non-solvent bath.[14–17] The isoporous surface, ideally featuring vertically-oriented cylinders, is formed in step (2) while step (3) is thought to vitrify and preserve the surface morphology while simultaneously generating the asymmetric structure in the supporting layer.

The design space of SNIPS membranes is notoriously vast; the rich formulation parameter space (block architecture, choice of solvent, molecular weight, etc.) coupled with an equally complex processing parameter space (evaporation time, temperature, etc.) presents significant hurdles in understanding structural evolution during SNIPS.[15,16,18] Experimental efforts have made progress in mapping out possible structures[19] and probing the dynamical evolution of the surface layer with grazing incident scattering techniques.[20,21] An empirical guide to choice of solvent was also reported by Sutisna *et al.*, providing much needed insight into the membrane design space.[22]

Despite this progress, exploring the vast design space is prohibitively expensive for experiments alone. Although nascent, computational studies have significantly clarified relationships between the design space and the thermal and kinetic processes that govern morphological development during SNIPS.[23–29] To this end, both particle-based[23,25–28] and field-based[24,27,29] methods have been employed. A pressing question that is at the cornerstone of SNIPS is under which conditions do vertically oriented cylinders appear in the

surface layer. Several computational studies demonstrated that the onset and orientation of cylindrical structures during solvent evaporation are highly dependent on evaporation rate and solvent selectivity for the majority hydrophobic block.[24–27] Dreyer *et al.* proposed a detailed explanation of cylindrical formation based on the successive layering of block copolymer micelles, whereby cylindrical elongation depends on proximity of a spherical aggregate's density to a critical value and orientation is dictated by the layer growth rate.[27]

While most computational investigations focus on structural evolution during the evaporation step, it was only very recently that diblock copolymer NIPS was studied.[29,30] The first workflow combining both the evaporation and NIPS step of SNIPS was introduced by Blagojevic *et al.* providing various insights into the interplay between the two steps.[30] A simpler approach that did not rely on simulating the evaporation step, focusing just on modeling NIPS, was proposed by Grzetic *et al.*[29] They demonstrated that through random phase approximation (RPA) one can determine which Flory-Huggins interaction parameters lead to the desired macrophase separated support layer. It was found that macrophase separation (necessary for the asymmetric structure) occured when the nonsolvent, for example water, is selective for the minority block, which is usually hydrophillic experimentally, and the solvent is selective for the hydrophobic majority block. An equilibrium self-consistent field theory (SCFT) simulation was used to generate the initial surface layer which was then stitched onto a film-bath interface, the resulting density profile being used to initialize a NIPS simulation. NIPS simulations were performed using dynamical self-consistent field theory (DSCFT), demonstrating that dense films are obtained when crossing a microphase instability as predicted with RPA, and an integral-asymmetric structure is obtained when a macrophase instability is crossed and glassy dynamics are imparted on the majority block.

In this study, we apply the workflow introduced by Grzetic *et al.* to investigate how the membrane morphology depends on various parameters. In particular, we find that the preservation of the ordering of pores in the selective layer and the connection between the selective layer and bulk microstructure is highly sensitive to both solvent and nonsolvent

selectivity. Choice of solvent is also found to impact the bulk microstructure. It is suggested that an optimal glass transition composition for the majority block exists that facilitates the formation of a surface-bulk connection and preservation of the surface ordering. Finally, we found that replacing more solvent with nonsolvent in the casting solution creates a more durable surface-bulk connection, yet distorts the orientation of cylindrical pores.

2. Simulation model and methods

2.1 Block copolymer model

We consider a linear block copolymer melt described by the field-theoretic partition function

$$Z_c = Z_0 \prod_{i=1}^{n} \int \mathcal{D}\rho_i \prod_{j=1}^{n} \int \mathcal{D}w_j \; e^{-\beta H[\{\rho\},\{w\}]} \tag{1}$$

where $\rho_i(\mathbf{r})$ is a fluctuating local segment density for species i, the $w_i(\mathbf{r})$ are a set of auxiliary fields introduced to decouple non-bonded pair interactions, and Z_0 is a constant that contains ideal gas terms and the density-explicit Hamiltonian is given by[31]

$$\begin{aligned} H[\{\rho\},\{w\}] =& \frac{1}{2\rho_0} \sum_{ij} \int d\mathbf{r} \chi_{ij} \rho_i(\mathbf{r}) \rho_j(\mathbf{r}) + \frac{\zeta}{\rho_0} \int d\mathbf{r} \left(\sum_i \rho_i(\mathbf{r}) - \rho_0 \right)^2 \\ &+ i \sum_i \int d\mathbf{r} \; w_i(\mathbf{r}) \rho_i(\mathbf{r}) - \sum_p n_p \ln Q_p[\{w\}] \end{aligned} \tag{2}$$

The overall monomer density is denoted by ρ_0, ζ is the Helfand compressibility parameter[32] which we fix to $\zeta = 25$, and n_p and $Q_p[\{w\}]$ are the number of molecules and single-molecule partition function, respectively, of molecular species p. In this work, we consider a single solvent S, a nonsolvent N, and a linear diblock copolymer P composed of monomeric species A and B, with A being the minority block. This represents a total of four monomeric species. Both the solvent and nonsolvent are taken to have degree of polymerization $N_S = N_N = 1$

while the diblock copolymer has $N_P = 50$. The single-chain partition functions for the solvent and nonsolvent are given by

$$Q_S = \frac{1}{V}\int d\mathbf{r}\, e^{-iw_S(\mathbf{r})}, \tag{3}$$

$$Q_N = \frac{1}{V}\int d\mathbf{r}\, e^{-iw_N(\mathbf{r})}, \tag{4}$$

where V is the system volume.

On the other hand, computing Q_P requires the successive building up of a chain with linker functions that embed the chain statistics, which we take to be discrete Gaussian. Given this, we compute Q_P with the following expression[31]

$$Q_P = \frac{1}{V}\int d\mathbf{r}^N \left[e^{-i\omega(\mathbf{r}_N)}\Phi(\mathbf{r}_N - \mathbf{r}_{N-1})e^{-i\omega(\mathbf{r}_{N-1})}\Phi(\mathbf{r}_{N-1} - \mathbf{r}_{N-2})\ldots e^{-i\omega(\mathbf{r}_2)}\Phi(\mathbf{r}_2 - \mathbf{r}_1)e^{-i\omega(\mathbf{r}_1)}\right] \tag{5}$$

where

$$\omega(\mathbf{r}_i) = \begin{cases} w_A(\mathbf{r}_i), & \text{if bead } i \text{ is of species } A \\ w_B(\mathbf{r}_i), & \text{if bead } i \text{ is of species } B \end{cases} \tag{6}$$

and $\Phi(\mathbf{r})$ is the discrete Gaussian chain linker function:

$$\Phi(\mathbf{r}) = \left(\frac{3}{2\pi b^2}\right)^{3/2} \exp\left(-\frac{3|\mathbf{r}|^2}{2b^2}\right), \tag{7}$$

Here, we assume the same statistical segment length b for both molecular species A and B. Since block copolymer membranes are universally fabricated using an asymmetric block copolymer to promote the formation of cylindrical phases, we set $N_A = 15$ and $N_B = 35$.

The Flory-Huggins interaction parameter χ_{ij} describes the local repulsive interaction between species i and j. We set the following default χ parameters unless otherwise specified: $\chi_{AB} = 0.8$, $\chi_{AN} = 0.5$, $\chi_{BN} = 1.5$, and $\chi_{NS} = 0.0$. The parameters χ_{AS} and χ_{BS} are systematically varied throughout this study. As demonstrated by Grzetic *et al.*, macrophase

separation may only occur when the nonsolvent is selective for the A block,[29] rationalizing our choice of $\chi_{BN} > \chi_{AN}$. Moreover, it is standard for the majority block to be hydrophobic and the minority block to be hydrophilic, such as with the extensively studied polystyrene-block- poly(4-vinylpyridine) (PS-P4VP) diblock copolymer,[14,17] further justifying our choice of χ_{BN} and χ_{AN}. A modestly large χ_{BN} value is chosen to provide a reasonably wide range of conditions that lead to macrophase separation.

In order to explore the effect of solvent selectivity on the overall morphology, we vary both χ_{AS} and χ_{BS} such that macrophase separation is always initiated upon the mass exchange of solvent and nonsolvent. We determine which χ values satisfy this condition by calculating the stability limit of a homogeneous phase of our three component $AB-S-N$ system using the random phase approximation (RPA). With the spinodal boundaries calculated using RPA, we can determine under which conditions a macrophase instability, microphase instability, or no instability (or the film is already unstable) is crossed during NIPS. We do this by assuming the average volume fraction of polymer in the film $\phi_P = n_P/(V\rho_0)$ is constant while S and N are exchanged, producing a linear trajectory in composition space. Finally, we identify which instability is crossed by determining whether the line of constant ϕ_P intersects a spinodal boundary marking a macrophase instability or microphase instability, or no instability (or the initial film composition is within the macrophase separation regime). The details of this calculation can be found in our previous work.[29]

Figure 1 displays the results of this RPA calculation by sweeping values of χ_{AS} and χ_{BS} for four different values of $\phi_P = (0.25, 0.2, 0.15, 0.1)$. Three regions are designated based on which instability is crossed during mass exchange with the specified χ_{AS} and χ_{BS} parameters: region IV leads to a film that is only microphase-separated, and thus nonporous, region III leads to a macrophase-separated, porous film upon the exchange of S and N, and region II indicates a film that undergoes bulk macrophase-separation even prior to mass exchange. We perform an array of 2D simulations with χ_{AS} and χ_{BS} values given by the points plotted in Figure 1, which are predicted to cause the film to undergo mass transfer-induced macrophase

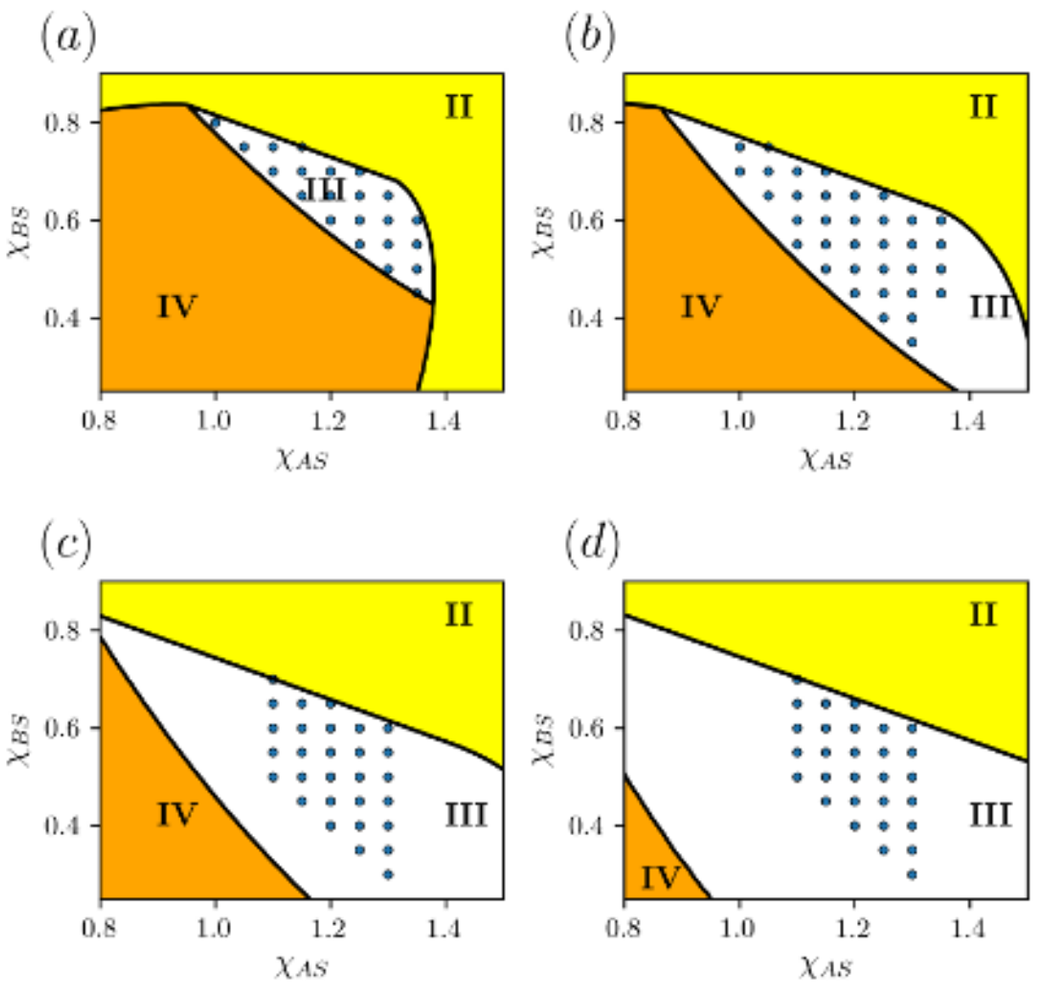

Figure 1: RPA stability map generated from solvent/nonsolvent exchange while sweeping χ_{AS} and χ_{BS} where (a) $\phi_P = 0.25$, (b) $\phi_P = 0.2$, (c) $\phi_P = 0.15$, (d) $\phi_P = 0.1$. Region I (not shown) denotes values of χ_{AS} and χ_{BS} which lead to no instability being crossed. Region II (yellow) indicates where the film is already unstable without needing to exchange solvent and nonsolvent. Region III (white) indicates where a macrophase instability is crossed. Region IV (orange) denotes values of χ_{AS} and χ_{BS} which lead to a microphase instability being crossed. The points scattered on each panel specify values of χ_{AS} and χ_{BS} with which simulations were performed, each of which predict mass transfer-induced macrophase separation in the film.

separation.

2.2 Dynamical self-consistent field theory (DSCFT)

The mesoscopic density fields $\rho_i(\mathbf{r}, t)$, for each species i, are evolved in time according to the following multicomponent diffusion equation

$$\frac{\partial}{\partial t}\rho_i(\mathbf{r}, t) = \nabla \cdot \left[\sum_j M_{ij}(\mathbf{r}; [\{\rho(t)\}])\nabla\mu_j(\mathbf{r}, t; [\{\rho\}])\right] \tag{8}$$

where $M_{ij}(\mathbf{r}; [\{\rho(t)\}])$ is a local and diagonal mobility matrix. The chemical potential $\mu_j(\mathbf{r}, t; [\{\rho\}])$ serves as the thermal driving force and is determined by our block copolymer model through the definition

$$\mu_j(\mathbf{r}; [\{\rho\}]) \equiv \frac{\delta F[\{\rho\}]}{\delta\rho_j(\mathbf{r}')} = \left\langle \frac{\delta H[\{\rho\}, \{w\}]}{\delta\rho_j(\mathbf{r}')} \right\rangle_{\{w\}} \tag{9}$$

where $\langle\cdots\rangle_{\{w\}}$ is a constrained average over the auxiliary chemical potential w fields. Although it is possible to sample the w fields stochastically with complex Langevin sampling,[33] we opt for a simpler approach where we approximate the average with the saddle-point configuration obtained from self-consistent field theory (SCFT)

$$\mu_j(\mathbf{r}; [\{\rho\}]) \approx \left.\frac{\delta H[\{\rho\}, \{w\}]}{\delta\rho_j(\mathbf{r}')}\right|_{\{w\}=\{w^*\}} \tag{10}$$

Therefore, at every time step we must solve for the saddle-point configuration $\{w^*\}$ that is self-consistent with the density fields $\{\rho\}$ computed at that time step. This approach of supplying thermodynamic information to eqn 8 using SCFT is termed dynamical self-consistent field theory (DSCFT).[34–38] Despite the cost of performing an SCFT loop every time step, we are able to leverage accurate SCFT block copolymer thermodynamics instead

of relying on a highly simplified Ginzburg-Landau type free energy functional typically used in phase-field simulations.[27,39–42]

The form of the mobility is given by the local coupling approximation[34]

$$M_{ij}(\mathbf{r};[\{\rho\}]) = \frac{k_B T}{\zeta_0 \gamma(\phi_B(\mathbf{r}))}\rho_i(\mathbf{r},t)\delta_{ij}, \tag{11}$$

where $k_B T$ is the thermal energy, ζ_0 is the friction coefficient of a molecule of either the solvent or nonsolvent species (assumed equal), and $\gamma(\phi_B(\mathbf{r}))$, a function of the local volume fraction of the B block $\phi_B(\mathbf{r}) = \frac{\rho_B(\mathbf{r})}{\rho_0}$, is a dimensionless enhancement of the friction at position $\mathbf{r}$ due to the presence of segments of the glassy B block. Garcia *et al.* demonstrated that glassy dynamics are crucial for obtaining an asymmetric porous structure in homopolymer-based membranes[42] and Grzetic *et al.* suggested this is also true for block copolymer membranes.[29] We impart glassy dynamics on the B block through $\gamma(\phi_B(\mathbf{r}))$ since it corresponds to the hydrophobic and glassy PS block used in experimental studies. In line with both Ref. 42 and 29, we adopt the following sigmoidal form of $\gamma(\phi_B(\mathbf{r}))$

$$\gamma(\phi_B(\mathbf{r})) = 1 + \frac{\gamma_B - 1}{1 + \exp\left(-\frac{1}{k}(\phi_B(\mathbf{r}) - \phi_B^*)\right)} \tag{12}$$

where γ_B is a dimensionless parameter that sets the friction enhancement upon crossing the glass transition composition, ϕ_B^*, the local volume fraction of block B at which the B block becomes glassy. Unless otherwise specified, we set $\phi_B^* = 0.6$. γ transitions from 1 to γ_B as the local volume fraction of B increases. For all simulations, we fix $\gamma_B = 10^4$, unless otherwise stated. The parameter k is the width of the sigmoid and is set to 10^{-3}. It is critical to note that these expressions imply that all components of the mobility M_{ij} crash to small values when

In order to implement eq. 8 numerically, we recast it into dimensionless form. The length scale of choice in our model is given by $\bar{b} = b/\sqrt{6}$ giving $\mathbf{r} = \bar{b}\tilde{\mathbf{r}}$, $\nabla = (\bar{b})^{-1}\tilde{\nabla}$, and $\tilde{\rho_0} = \rho_0(\bar{b})^3$. All time-dependent factors in our dynamic equation will be rescaled by the

time scale $\tau = (\bar{b})^2 C/D_{rouse}$ where D_{rouse} is the diffusion coefficient for Rouse-like chains and $C = \tilde{\rho}_0/N$ is the dimensionless polymer chain number density. Using the definition $D_{rouse} \equiv k_B T/\zeta_0 N$, the time scale can be expressed in terms of the Rouse time of the copolymer as $\tau = \frac{\tilde{\rho}_0(\bar{b})^2\zeta_0}{k_B T} = \frac{\tilde{\rho}_0\pi^2}{2N_P^2}\tau_R$. In this work we present length and time scales in terms of the copolymer radius of gyration, $R_g = \sqrt{50}\ \bar{b}$, and the Rouse time τ_R. Due to the stiffness of eq. 8, we apply an exponential time differencing (ETD) [43,44] scheme to propagate the densities forward in time. We use an adaptive time-stepper to mitigate time-step-error induced negative densities that lead to divergent trajectories; the details may be found in the Supporting Information.

The inner SCFT calculation to find the saddle-point configuration $\{w^*\}$ was performed using a first order semi-implicit algorithm (SI1). [44,45] Different tolerances on the L2-norm of the residuals of the w fields were used for different parts of the simulation workflow and are stated in the following section.

2.3 SNIPS simulation setup

As mentioned before, the SNIPS process involves the casting of a block copolymer solution, evaporating the solvent(s) from the film inducing the self-assembly of block copolymers at the surface, and finally immersing the film into a non-solvent bath causing the bulk of the film to undergo macrophase separation. In lieu of modeling each step of this complex process, we apply a simplified workflow introduced by Grzetic *et al.* [29] which eliminates the dry evaporation step, replacing it by a specified ordered surface that serves as an initial condition for a NIPS simulation of the wet immersion step. By avoiding an explicit simulation of the evaporation step, we significantly reduce the computational cost of a single simulation, allowing us to more easily perform the wide parameter sweeps featured in this work. We further assume that the bulk of the film remains homogeneous, effectively stipulating that no micelles form in the bulk during the casting or evaporation step. Thus the main step we are simulating is the exchange of non-solvent and solvent at the film-bath interface where

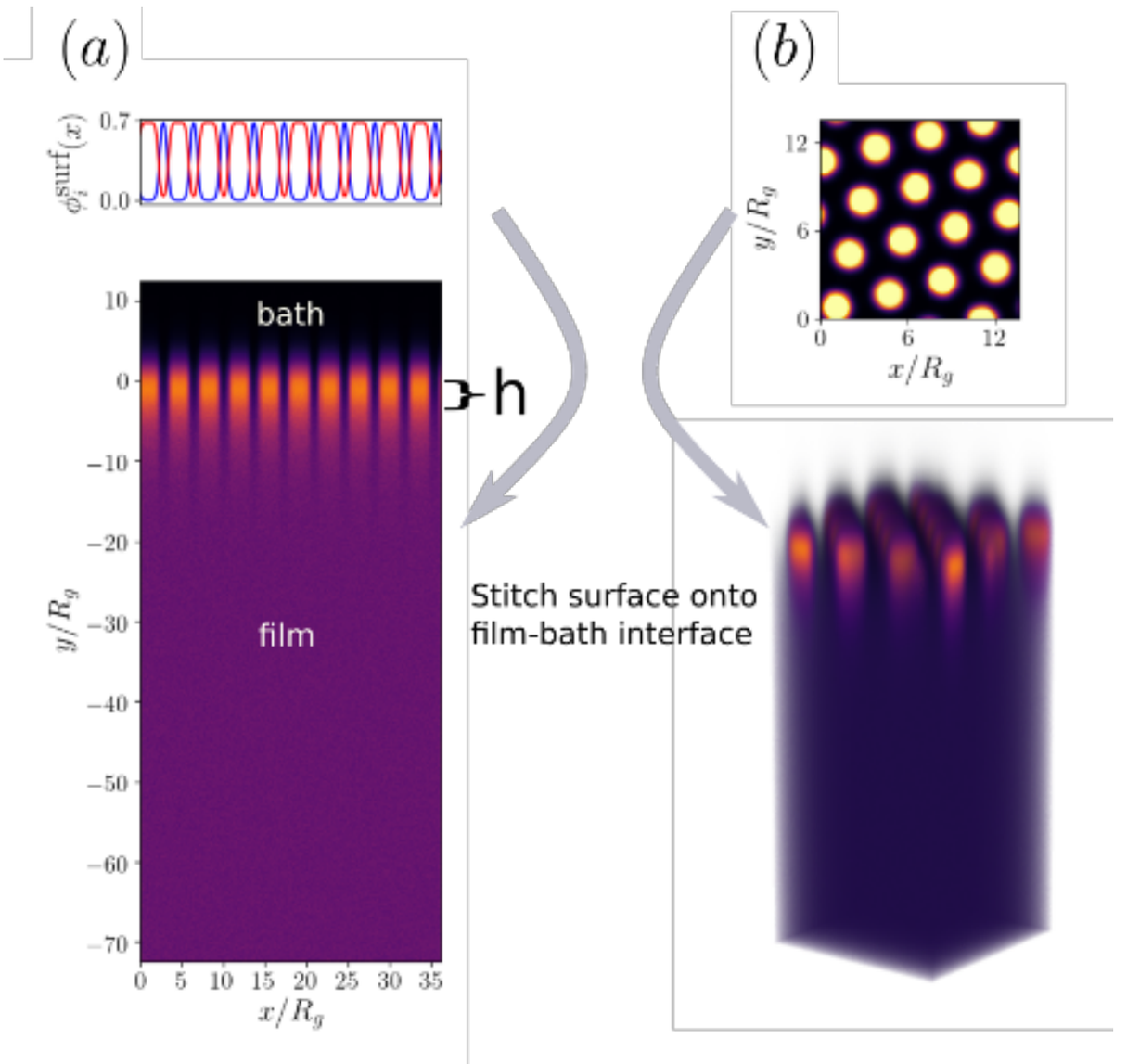

Figure 2: Illustration of workflow to model the SNIPS process in dimension $d = 2$ (left) and $d = 3$ (right). First, an equilibrium SCFT simulation is performed to obtain the surface profile that mimics an isoporous surface generated from an evaporation step. A second SCFT simulation provides the density and auxiliary fields of a converged film-bath interface. The results are then stitched together, giving the initial condition to the SNIPS simulation. The 1D SCFT simulation on the left plots the A block (blue lines) and B block (red lines) densities. The 2D initial condition for the SNIPS simulation plots the B density. The 2D SCFT simulation and 3D SNIPS initial condition on the right display the A density.

the film has an isoporous surface, assumed to originate from the evaporation step. We note it is possible an explicit evaporation simulation may yield a significantly different surface morphology than the approximated one. For example, while we employ a vertically oriented cylindrical structure, an explicit evaporation simulation may yield parallel cylinders. Since parallel cylinders are undesirable as the surface morphology, we tacitly assume all simulation parameters promote the formation of vertically oriented cylinders during the evaporation step.

We accomplish this workflow within our DSCFT framework in the following way, illustrated in Figure 2. For a DSCFT SNIPS simulation in d dimensions, we approximate the ordered surface with a density profile that results from an equilibrium SCFT simulation in $d-1$ dimensions. We denote the surface composition as $\{\phi^{(\text{surf})}(x)\}$ or $\{\phi^{(\text{surf})}(x,y)\}$, respectively, for $d=2$ or $d=3$. The bulk values of each species used for all simulations are $\phi_P^{(\text{surf})}=0.6594$, $\phi_S^{(\text{surf})}=0.3361$, and $\phi_N^{(\text{surf})}=0.0045$, approximating a surface profile nearly absent of any nonsolvent with polymer concentration high enough to guarantee microphase separation.

Following the $d-1$ dimensional SCFT simulation of the surface profile, we run a d dimensional SCFT simulation to obtain the saddle-point configuration of the $\{w\}$ fields that match the $\{\phi\}$ fields corresponding to a film in contact with a bath, denoted as $\{w^{(\text{film-bath})}(x,y)\}$ and $\{\phi^{(\text{film-bath})}(x,y)\}$, respectively, when $d=3$. We introduce a small noise perturbation to the d dimensional SCFT simulations to break the symmetry along axes orthogonal to the film surface normal. The function $\Theta(z)=\frac{1}{2}\left[\tanh\left(\frac{z-z_{int}}{\lambda}\right)+1\right]$ modulates the interface between the film and the bath, placing the interface at $z=z_{int}$, with an interfacial width λ. For the $d=2$ case, we selected $\lambda=15\bar{b}\approx 2.1R_g$ to provide a smooth film-bath interface which improves stability. When $d=3$, we employed $\lambda=7.5\bar{b}\approx 1.1R_g$ as it was found that broader interfacial widths consistently resulted in the loss of surface order. The L2-norm of the residuals for the $d-1$ dimensional SCFT surface profile simulation and the d dimensional SCFT film-bath simulation were converged within a tolerance of 10^{-5} using the SI1

algorithm.

Finally, in the case $d = 3$, the resulting density fields $[\{\phi^{(\text{surf})}(x,y)\}, \{\phi^{(\text{film-bath})}(x,y)\}]$ and auxiliary chemical potential fields $[\{w^{(\text{surf})}(x,y)\}, \{w^{(\text{film-bath})}(x,y)\}]$ are stitched together to form the initial condition of the DSCFT SNIPS simulations which model the NIPS step of the SNIPS process.

The overall initial composition profile is then given (in $d = 3$) by

$$\begin{aligned}\phi_i(\mathbf{r}) = &\left[\phi_i^{(\text{film-bath})}(x,y) + \Lambda(z)\left(\phi_i^{(\text{surf})}(x,y) - \phi_i^{(\text{film-bath})}(x,y)\right)\right](1-\Theta(z)) \\ &+ \phi_i^{(\text{film-bath})}(x,y)\Theta(z),\end{aligned} \tag{13}$$

where z is the direction normal to the film-bath interface. Eqn 13 is used for each species except for the non-solvent, which is determined using the incompressibility condition $\phi_N(\mathbf{r}) = 1 - \sum_i^{n-1}\phi_i(\mathbf{r})$. Here, it has been assumed that we have n species including a non-solvent, at least one solvent, and at least one diblock copolymer. The function $\Lambda(z) = \exp\left[\frac{z-z_{int}}{h}\right]$ modulates the transition between the bulk of the film and the ordered surface layer, which is placed at the film-bath interface with a thickness h; as z decreases, proceeding away from the film-bath interface, $\Lambda(z)$ serves to exponentially dampen $\phi_i^{(\text{surf})}(x,y) - \phi_i^{(\text{film-bath})}(x,y)$ such that in the bulk of the film, $\phi_i(\mathbf{r}) \to \phi_i^{(\text{film-bath})}(x,y)$. All simulations in this work were performed with $h = 25\bar{b} \approx 3.5R_g$.

The cell dimensions for the $d = 2$ SNIPS simulations are $256\bar{b} \times 2048\bar{b} \approx 36.2R_g \times 289.6R_g$ with grid spacing $\Delta x = \Delta y = 1\bar{b} \approx 0.14R_g$. For large χ_{AS} values, the simulations were run with $\Delta y = 0.5\bar{b} \approx 0.07R_g$ to improve stability. The dimensions for the $d = 3$ simulations are $96\bar{b} \times 96\bar{b} \times 800\bar{b} \approx 13.6R_g \times 13.6R_g \times 113.1R_g$ with $\Delta x = \Delta y = 1.5\bar{b} \approx 0.21R_g$ and $\Delta z = 1.562\bar{b} \approx 0.22R_g$. In a few instances, $\Delta z = 25/24\bar{b} \approx 0.15R_g$ was used to improve stability. Eq 8 was solved using periodic boundary conditions, meaning the film and bath have a mirror image about the center of the longest cell dimension. The dynamical time-step used was $\Delta t \sim 3.9 \times 10^{-5}\tau_R$ unless an adaptive time-stepper was employed. The L2-norm of the residuals for the inner saddle-point loop of the SNIPS simulations were converged within

a tolerance of 10^{-5} or 25 iterations were performed using the SI1 algorithm. The dynamic time-step was set to $\Delta t = 0.02\tau \approx 4 \times 10^{-5}\tau_R$

Each 2D simulation was run until the glassy front, the deepest part of the film where at least one grid point is glassy, was $400\bar{b} \approx 56.6R_g$ below the top of the film, which is defined as the highest (closest to the bath) part of the film featuring at least one grid point that was glassy. Due to the bottom of one film connecting with the bottom of its mirror image, the last $100\bar{b} \approx 14.1R_g$ section of the film is significantly affected by finite size effects, hence we do not perform analysis on this part of the film. For 3D simulations, we only ensure the glassy front reaches halfway through the film since we use these mainly to investigate how the surface layer connects with the bulk morphology.

3. Results and discussion

3.1 2D simulations

3.1.1 Solvent selectivity

Previous investigations, both experimental[22,46] and computational,[24–27] demonstrated the importance of solvent selectivity on the surface layer morphology fabricated with SNIPS. These studies, however, provided little insight into how solvent selectivity impacts the structure of the supporting layer that forms during the NIPS step.

Two morphologies with different solvent selectivities can be found in Figure 3. The top row shows the time evolution of a morphology generated with a modestly selective solvent ($\chi_{AS} = 1.1$ and $\chi_{BS} = 0.75$) while the bottom row morphology was formed with a substantially more selective solvent ($\chi_{AS} = 1.25$ and $\chi_{BS} = 0.6$). We note that the size of the nonsolvent-rich domains is similar to that of the polymer microdomains. This is due to the fact that the simulated films are 100 nm deep, while experimental membranes are typically 10 - 100 μm thick. Since nonsolvent-rich domains formed via NIPS increase in

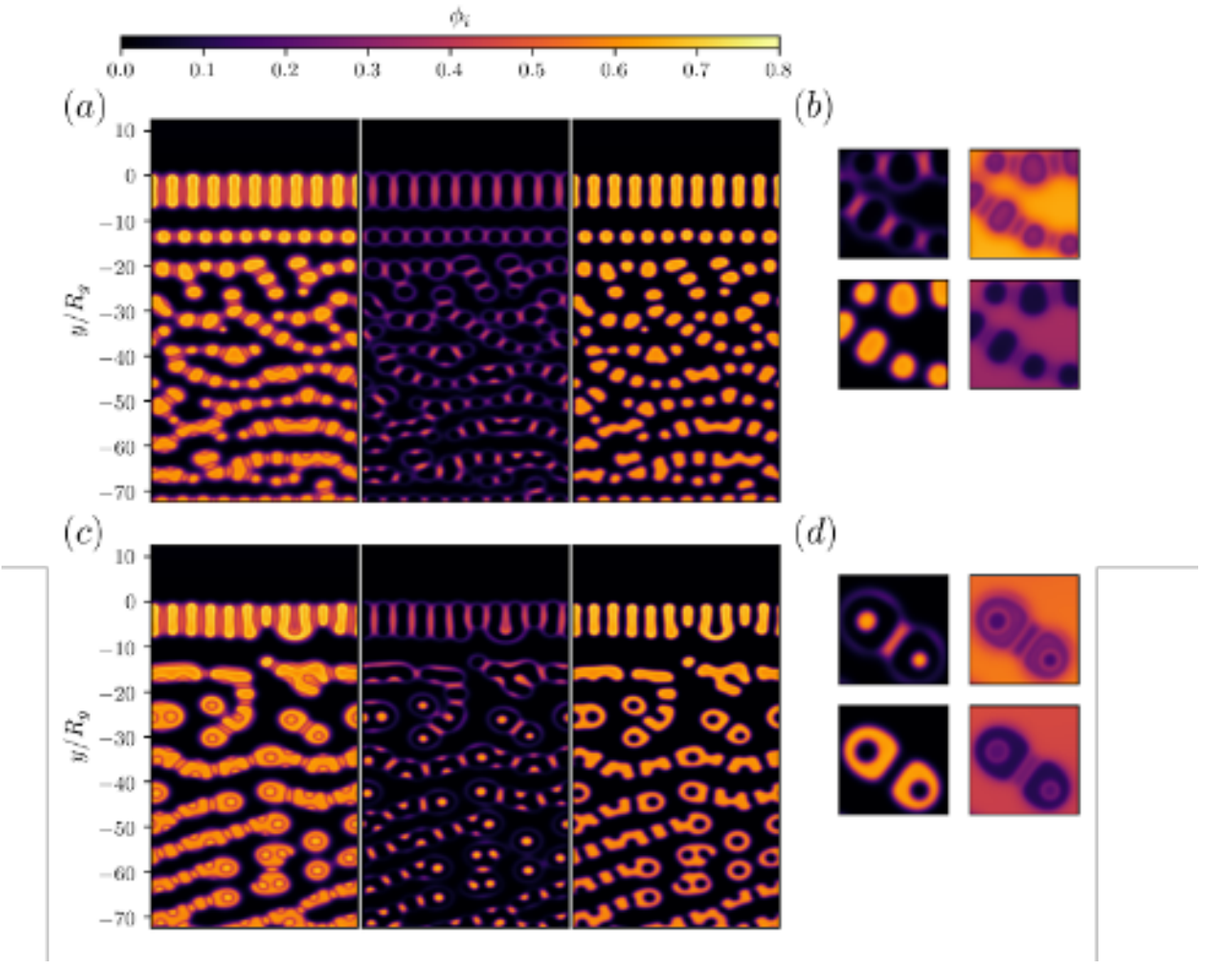

Figure 3: (a) Total polymer density $\phi_P(\mathbf{r},t) = \phi_A(\mathbf{r},t) + \phi_B(\mathbf{r},t)$ (left), A block density $\phi_A(\mathbf{r},t)$ (center), and B block density $\phi_B(\mathbf{r},t)$ (right) of a morphology generated from a SNIPS simulation with $\chi_{AS} = 1.1$ and $\chi_{BS} = 0.75$. (b) Zoomed in region of the film from $x = 20R_g$ to $x = 30R_g$ and from $y = -40R_g$ to $y = -30R_g$ showing the (top left) A block density, (bottom left) B block density, (top right) S density $\phi_S(\mathbf{r},t)$, and (bottom right) N density $\phi_N(\mathbf{r},t)$. (c) Total polymer density (left), A block density (center), and B block density (right) of a morphology generated from a SNIPS simulation with $\chi_{AS} = 1.25$ and $\chi_{BS} = 0.6$. (d) zoomed in region of the film from $x = 22R_g$ to $x = 32R_g$ and from $y = -32R_g$ to $y = -22R_g$ showing the (top) A block density and (bottom) B block density. Snapshots in (a) and (b) were taken at time $t \approx 210\tau_R$ and snapshots in (c) and (d) were taken at time $t \approx 320\tau_R$. Both have polymer film concentration $\phi_P = 0.25$. The zoomed in regions show an example of what we denote (b) AB micelles and (d) ABA vesicles.

size with film depth, simulations of thicker films will show appreciably larger nonsolvent-rich domains. However, due to computational limits, we could not simulate a large enough film to observe a significant separation of the macro and micro-phase separation length scales.

The two final structures have significant differences. The modestly selective solvent produced a structure composed of strung together crew-cut micelles, similar to that reported in our previous work.[29] Since the micellization is induced by the introduction of nonsolvent, the hydrophilic A block forms the corona and is ultimately responsible for 'gluing' together different micelles to form the membrane matrix. This can be seen from the panels displaying the A density, the most dense regions of A establish bridges between B cores which are responsible for the holding the membrane structure in place due to its glassy nature. From here on out, we refer to these crew-cut micelles as "AB micelles" since the A block forms the corona and the B block forms the core of the micelle.

The more selective solvent in the case of Figure 3b forms a structure consisting of micelles bridged together by the A block. In contrast to the moderately selective case, however, micelles produced by the more selective solvent feature an A block inner core which is surrounded by a B block outer core. These micelles are actually vesicles[47,48] since the hydrophilic A block in the core is slightly swollen with nonsolvent as depicted in Figure 3d. For convenience, we label these as "ABA vesicles" as we have an A corona, a B outer core, and an A inner core.

In order to determine under which conditions ABA vesicles or AB micelles emerge, we varied the parameters χ_{AS}, χ_{BS}, and ϕ_P as seen in Figure 1. Figure 4 presents the set of parameters that give rise to ABA vesicles and the number of ABA vesicles that appear. Some simulations resulted in a glassy skin forming below the surface, preventing nonsolvent from entering the rest of the film and inducing phase separation. We expect that adding thermal noise might allow the skin to be perforated by nonsolvent; however we leave this for future work.

It is evident that increasing the polymer film concentration ϕ_P provides more χ_{AS} and χ_{BS}

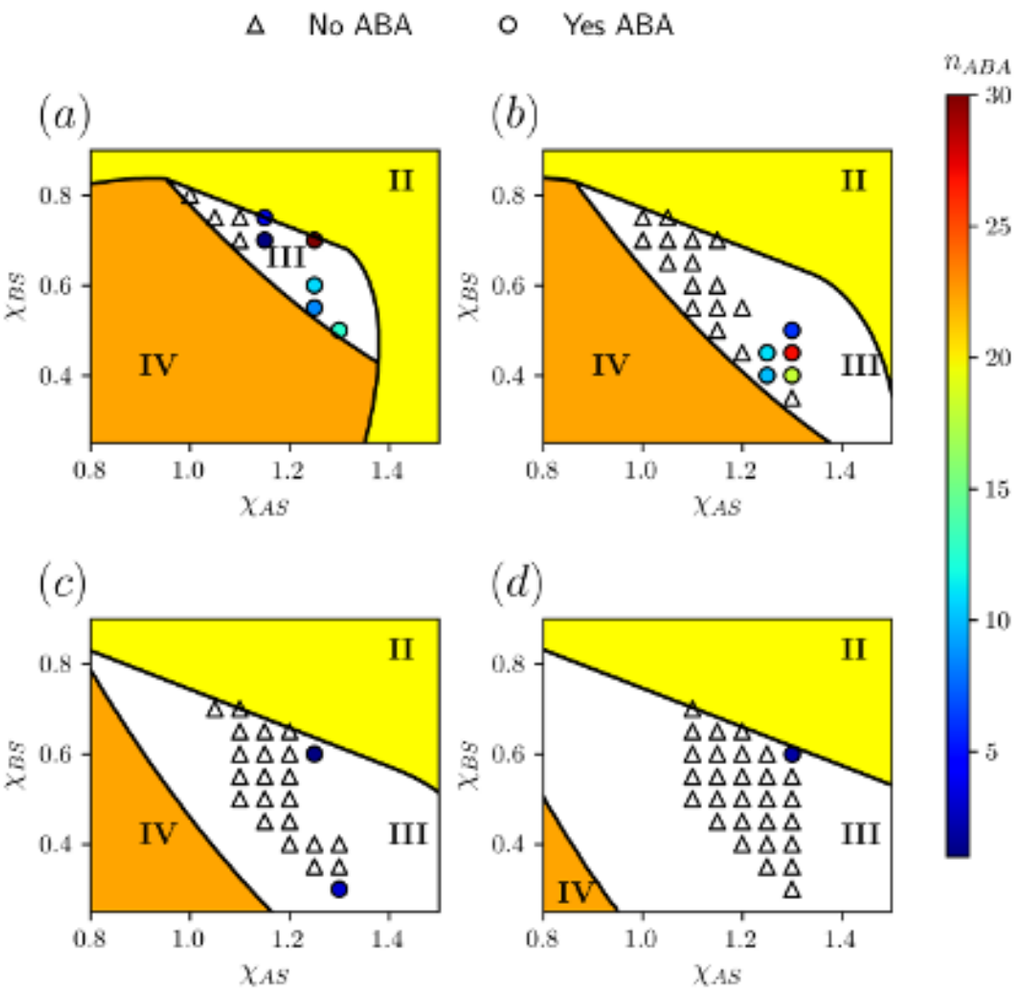

Figure 4: Conditions under which ABA vesicles appear in the film microstructure overlaid on top of RPA stability maps generated from sweeping χ_{AS} and χ_{BS} where (a) $\phi_P = 0.25$, (b) $\phi_P = 0.2$, (c) $\phi_P = 0.15$, (d) $\phi_P = 0.1$. Regions I, II, and III correspond to the same instabilities described in Figure 1. Points marked with a triangle marker indicate no ABA vesicles appeared in the final structure, and thus only AB micelles form the membrane matrix, and points marked with a circle marker indicate ABA vesicles did appear in the final structure. The interior color of each circle corresponds to how many ABA vesicles were observed. Pairs of χ values that are unmarked in this figure but marked in Figure 1 refer to simulations that either formed a glassy skin, preventing mass-exchange throughout the whole film, or that we were unable to run stably.

values that lead to the formation of ABA vesicles. When $\phi_P = 0.1$ (Figure 4d) and $\phi_P = 0.15$ (Figure 4c), ABA vesicles are extremely difficult to obtain, and when they do appear it is only a small number of them, hence the film morphology is constructed primarily from AB micelles. This is consistent with previous experimental investigations, which reported an increase in polymer concentration induced the formation of vesicles.[48–50]

Aside from ϕ_P, large values of χ_{AS} drive the formation of ABA vesicles. The exact value χ_{AS} must be for ABA vesicles to appear depends on ϕ_P: the larger ϕ_P is, the less χ_{AS} needs to be to obtain ABA vesicles. This observation is reasonable, the more unfavorable the interaction between the A block and S is prompts the A block to minimize contact with S by populating an inner core depleted of S but partially swollen with the more favorable N. Figure 3d demonstrates that very little S enters the inner core and mainly resides in the exterior region that is in contact with the A corona. Furthermore, increasing ϕ_P increases the strength of interaction between the A block and solvent, explaining why ABA vesicles appear under a wider range of χ_{AS} values at larger ϕ_P.

Whether the microstructure consists of AB micelles or ABA vesicles may have substantial ramifications on the membrane performance. It can be seen that the AB micelle matrix has many hydrophilic A block bridges which provide additional avenues of N diffusion aside from just the polymer-poor porous regions. This can be seen in the bottom right panel in Figure 3b where the N density in the A bridges is not much less than in the pores. The existence of these bridges may help explain why block copolymer membranes can offer greater water permeance compared to their homopolymer counterparts.[12] However, when the foundation of the microstructure is fused ABA vesicles, much of the A block is relegated to the inner core. This makes the ABA vesicles bulkier and reduces the number of A bridges in the overall morphology, consequently restricting the diffusion of N.

Finally, we note that the formation of crew-cut micelles, while consistent with our previous work,[29] is in conflict with Blagojevic *et al.*, where the reported micelles had the majority block formed the corona instead of the core.[30] Blagojevic *et al.* employed $\chi_{NS} = -50$ and

a mobility that gradually decreases with $\phi_B(\mathbf{r})$. In contrast, we chose $\chi_{NS} = 0$ for all simulations and used a sharp sigmoidal mobility model that only decreases meaningfully upon approaching the glass transition composition. Therefore, the phase separation front in Blagojevic *et al.* is expected to be slightly faster, yet with a less mobile B block compared to our work. We hypothesize that conventional micelles in Blagojevic *et al.* did not have enough time to "invert" to form the crew-cut motif that we found in our previous and current work. A more detailed investigation of this issue is left for future work.

3.1.2 Polymer concentration

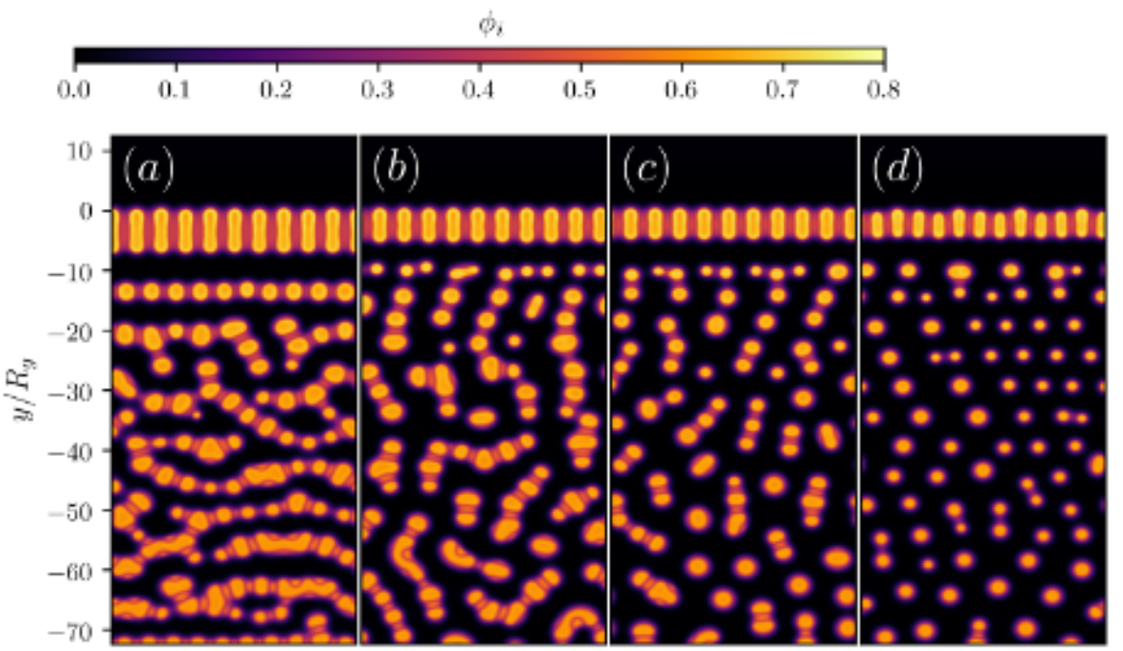

Figure 5: Total polymer density of a morphology generated from a SNIPS simulation with $\chi_{AS} = 1.1$ and $\chi_{BS} = 0.75$ with polymer volume fraction in the film (a) $\phi_P = 0.25$, (b) $\phi_P = 0.2$, (c) $\phi_P = 0.15$, (d) $\phi_P = 0.1$. Each snapshot was taken at time $t \approx 210\tau_R$.

Figure 5 displays snapshots of the total polymer density taken at time $t \approx 210\tau_R$ for four different values of polymer volume fraction in the film $\phi_P = [0.25, 0.2, 0.15, 0.1]$. In the case where $\phi_P = 0.1$, the bulk structure largely consists of disconnected circular micelles.

The finite amount of polymer prevents a sufficient number of micelles from forming, leaving mainly single micelles and a few connected micelles. Such a morphology cannot be expected to form a proper support layer in an experimental membrane; once the nonsolvent is drained from the membrane, the entire structure will collapse.

Upon increasing ϕ_P, we begin to see individual spherical micelles combine to form a pearl-like structure which was previously reported by Grzetic *et al.*[29] As noted in the previous section, the A block forms the bridge that connects individual micelles in the pearl-like structure. The length then depends on how many micelles can fuse together which increases with ϕ_P. We find when $\phi_P = 0.25$, there are enough micelles glued together to form a complete and connecting polymer-rich matrix. For this set of interaction parameters, polymer film concentrations less than $\phi_P = 0.25$ fail to form long enough pearl-like structures to construct a connected matrix. This is consistent with our previous work where 2D morphologies at $\phi_P = 0.2$ were composed of disconnected pearl-like structures. We remark that the conditions necessary for connectedness may differ in 3D, however we do not investigate this here.

This observation is not consistent with experiments where fully connected membranes were fabricated at polymer volume fractions in the range of $\sim \%15 - 25$ for the casting solution.[17,19,20,46] One significant difference between our work and real systems is the repulsive strength between the hydrophobic B block and the nonsolvent N. Calculating $\chi_{PS-water}$ using the Hansen solubility parameters for both PS and water at 298 K results in a much larger value than we are able to model: $\chi_{PS-water} \approx 15$.[51] Furthermore, much larger molecular weights are used $N_P \sim 1000$.[17,19,20,46] Our current values of $\chi_{BN} = 1.5$ and $N_P = 50$ do not punish $B - N$ interactions nearly as much as in experimental systems, which may allow many micelles to remain disconnected. Connecting micelles together decreases the overall contact of B with N; although the B block forms the core, N swells the A corona thus contacting B. Currently, we are unable to model such large interactions so we leave investigating increasing N_P and χ_{BN} for future work.

One notable feature of the morphologies seen in both Figure 3 and 5 is the lack of connection between the isoporous surface and the rest of the membrane. In 2D, the surface must form a lamellar structure so that the pores formed by the A block are oriented along the film surface normal. However, due to the asymmetry in block lengths and solvent selectivity, the block copolymer in the initial film would prefer to form hexagonally packed droplets with an A core encased in a B matrix. The primary mechanism that stabilizes the lamellar sheets is the glassy behavior of the B block, although even if it wasn't glassy, the non-equilibrium nature of the mass transfer may allow some of the surface to remain lamellar. An example can be found in Grzetic *et al.*, where simulations with and without glassy dynamics found part of the surface connected with the sublayer.[29] In general, however, structural frustration and the ingress of nonsolvent largely prevents the extension of the lamellar sheets in the initial stages of mass transfer-induced phase separation, creating a gap between the surface and the initial polymer-rich domains nucleated due to the introduction of N in the film.

3.2 3D simulations

We have previously discussed the structural frustration that occurs when approximating an isoporous surface in 2D and its impact on the connectivity with the sublayer below. Therefore, we perform a select number of simulations in 3D to investigate how various parameters affect the membrane structure, with particular attention paid to the selective layer morphology and its connection to the bulk. In each case, a hexagonally packed lattice of pores at the top surface was obtained by a 2D SCFT simulation, which we anticipated would alleviate structural frustration in the surface during mass exchange. Figure 6a presents the spinodal boundaries for three systems that correspond to the pair of χ values: $\{(\chi_{AS}, \chi_{BS})\} = \{(1.0, 0.8), (1.1, 0.7), (1.2, 0.6)\}$ with $\chi_{AN} = 0.5$ as was used in the 2D simulations. Figure 6b presents the same but using $\chi_{AN} = 1.0$. Different film compositions were also used as indicated by the points. In this section, we probe the effect of the following four parameters on the 3D morphology: solvent selectivity, hydrophilicity of the A block,

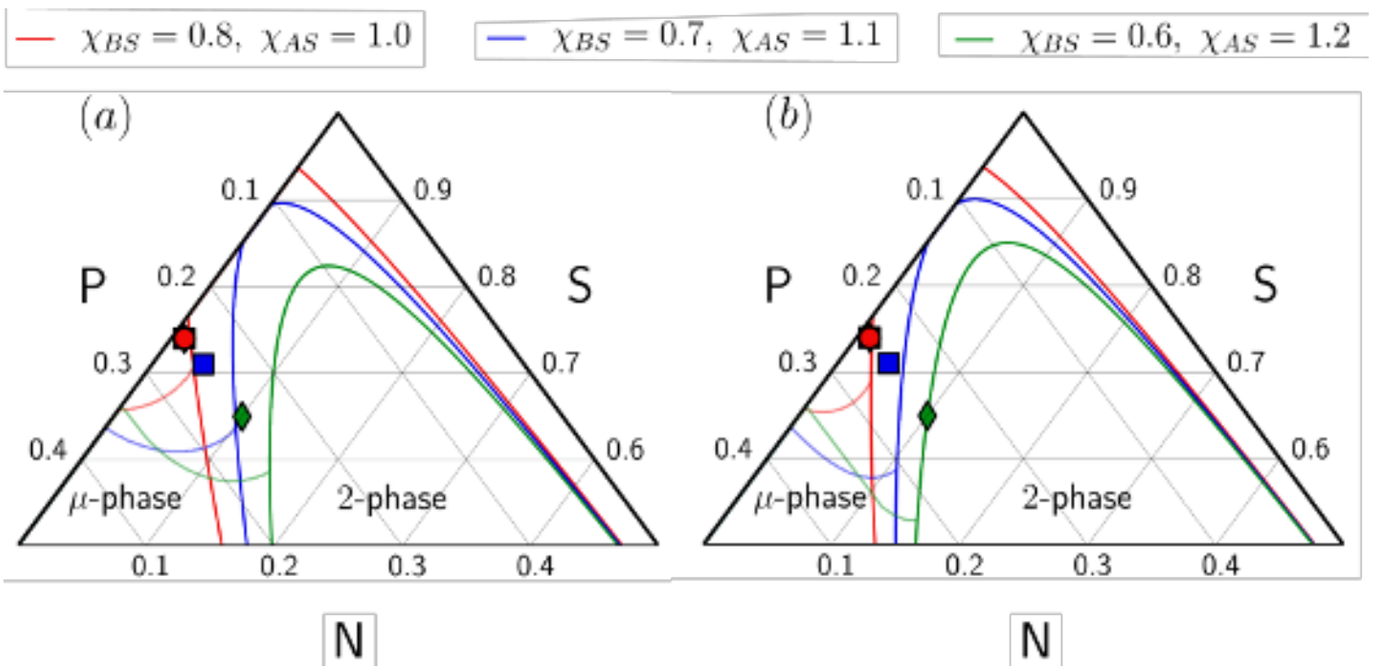

Figure 6: Zoomed in view of a ternary phase diagram for the AB diblock, S solvent, and N nonsolvent with (a) $\chi_{AN} = 0.5$ and (b) $\chi_{AN} = 1.0$. Spinodals corresponding to a macrophase or microphase instability are plotted with dark or light lines, respectively. The points represent the initial film compositions of various simulations performed: $\{(\phi_P, \phi_S, \phi_N)\} = \{(0.25, 0.74, 0.01), (0.25, 0.71, 0.04), (0.25, 0.65, 0.1)\}$. Red lines and circles are used to display the spinodals and initial film compositions, respectively, for $(\chi_{AS}, \chi_{BS}) = (1.0, 0.8)$. Blue lines and squares are used for $(\chi_{AS}, \chi_{BS}) = (1.1, 0.7)$. Green lines and diamonds are used for $(\chi_{AS}, \chi_{BS}) = (1.2, 0.6)$

.

initial film composition, and the glass transition composition of the B block. Each effect is discussed in an individual subsection, with the last subsection providing additional insight into surface-bulk connectivity.

3.2.1 Solvent selectivity

Figure 7 presents the results of varying the pair (χ_{AS}, χ_{BS}) on the time evolution of the film microstructure. We begin by turning our attention towards the final morphology of the membrane surface seen in the last panel of Figure 7a, b, and c. When $(\chi_{AS}, \chi_{BS}) = (1.2, 0.6)$ and $(\chi_{AS}, \chi_{BS}) = (1.1, 0.7)$, the initially isoporous surface is significantly deformed during the NIPS process. The final pore sizes are no longer uniform and the original hexagonal packing of the A cylindrical cores is lost. The A block density profile reveals that many of the cylindrical pores have collapsed, explaining the lack of order at the top surface. Although it is largely assumed in the literature that the NIPS step kinetically traps the surface structure,[15] this has not been proven to be true in every membrane-forming system. It has been reported that the ordering seen in the casting solution differed from that seen in the membrane's selective layer, with structural rearrangement during NIPS proposed as a possible explanation.[52]

We previously mentioned that in 2D, structural frustration occurs since we force the pores to be lamellar instead of the preferred hexagonal packing. It is clear, however, that additional elements of structural frustration are present in 3D that cannot be explained by the cell dimension. Instead, we attribute this to the difference in thermodynamic environments prior to and during mass-exchange. Initially, the top surface contains very little N, and so the block copolymer is mainly solvated in S which is selective for the B block promoting the hexagonal packing of A cores. However, N is selective for the A block, and so as more N diffuses into the surface, the cylinders expand and begin to fuse together, leading to the collapse of several pores. A similar observation was reported by Blagojevic *et al.* where the vertical cylinders swelled upon the exchange of N and S.[30] Their simulations, however,

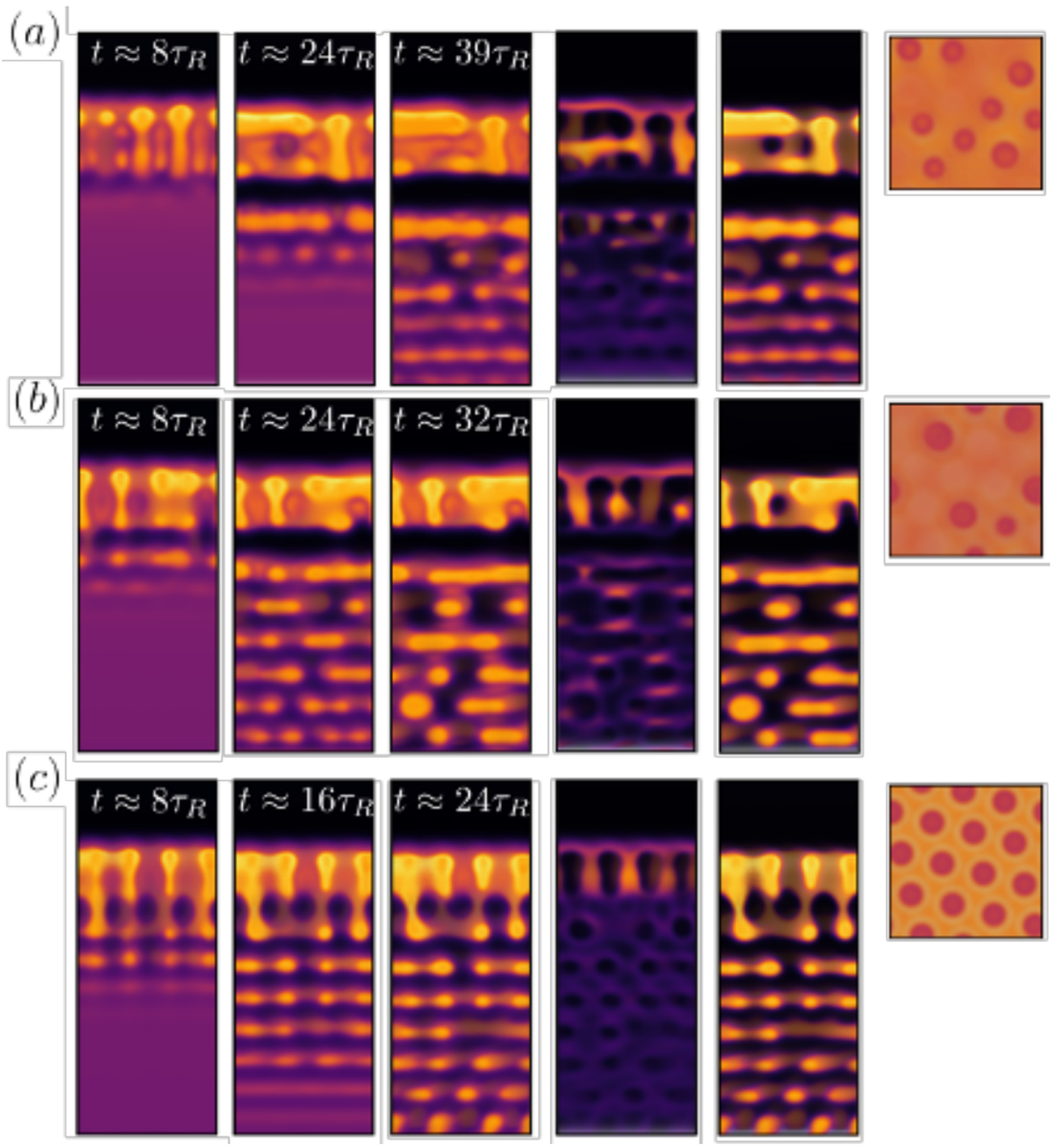

Figure 7: Time evolution of a morphology generated from a SNIPS simulation with $\chi_{AN} = 0.5$ and (a) $(\chi_{AS}, \chi_{BS}) = (1.2, 0.6)$, (b) $(\chi_{AS}, \chi_{BS}) = (1.1, 0.7)$ and (c) $(\chi_{AS}, \chi_{BS}) = (1.0, 0.8)$. The first five panels show a cross section of the film morphology and the last panel shows a top down view of the surface. The first three panels display $\phi_P(\mathbf{r}, t)$, the fourth displays $\phi_A(\mathbf{r}, t)$, the fifth panel displays the B block density $\phi_B(\mathbf{r}, t)$, and the last panel displays $\phi_P(\mathbf{r}, t)$. Snapshots of the total polymer density are labeled according to the Rouse time at which they were taken. Panels displaying the A and B block densities and the top down view of the surface correspond to the latest time shown in the time evolution.

employed a larger χ_{BN} value which we hypothesize constrains the swelling of the cylinders, prevent the pores from collapsing. Furthermore, as S becomes more selective for B, further swelling it, the propensity for N to enter the B domain increases.

This explains why when $(\chi_{AS}, \chi_{BS}) = (1.0, 0.8)$, the system with the least selective solvent, we obtain the least structural deformation. More solvent is present in the pore-forming A domain, screening the $A - N$ interaction, which facilitates the diffusion of N towards the pores rather than the B domain. This also increases the density of the B-rich domains, providing faster vitrification and a stronger repulsion towards N. We anticipate that larger values of χ_{BN} can stabilize the B domain and enable more selective solvents to be used in the casting solution.

Additionally, we observe when $(\chi_{AS}, \chi_{BS}) = (1.2, 0.6)$ and $(\chi_{AS}, \chi_{BS}) = (1.1, 0.7)$ the isoporous surface is disconnected from the bulk of the film. It is clear when $t = 8\tau_R$, the cylinders begin to extend into the film. However, at some point during the early structural development, these extensions are pinched off. The structural integrity of these extensions is granted by the vitrification of the B block, thus, the increase in χ_{BS} should repel S from entering the B domains allowing it to vitrify. Furthermore, we can see the bulk microstructure recede from the surface over time. During NIPS, N does not generally fill the entire volume previously occupied by S; polymer also moves into to fill that volume which causes the film to shrink, a phenomenon also reported in homopolymer NIPS.[53] This shrinking is responsible for the recession of the bulk film from the surface - the surface is held in place by the glassy B block while the film has not yet vitrified. The connectivity of the surface layer is undoubtedly influenced by the relatively small lateral cell size imposed by computational limitations; nonetheless, we believe these qualitative parametric trends to hold irrespective of system size.

The time evolution of the morphologies also demonstrates the difference in formation kinetics upon varying solvent selectivity. Phase separation speed is seen to increase as solvent selectivity decreases; at $t \approx 8\tau_R$, the least selective solvent system is beginning to

form the third layer in the bulk microstructure while the most selective solvent system has not even formed its first layer. The speed at which the film phase separates is determined by how well N and S are able to exchange and how much N is required to induce phase separation. Since N enters the film predominantly through A-core cylinders, $N-S$ exchange should proceed faster as χ_{AS} is decreased. Furthermore, since the A block forms the corona in the bulk microstructure, a smaller χ_{AS} will facilitate the transport of S out of the film and guide more N into the film. Finally, the spinodals for each system plotted in Figure 6 reveal that the more selective the solvent, the closer the 2-phase region is from the initial film compositions and thus the less N needs to enter into the film to induce phase separation.

We conclude this subsection with an examination of the bulk microstructure. A clearer depiction of the final microstructure is seen in Figure SI1. The trend where a larger χ_{AS} value induces the formation of ABA vesicles is extended to 3D morphologies as well: as χ_{AS} increases, the A block becomes more segregated, forming increasingly dense regions of A. It is difficult to claim these dense regions of A block form the inner core of ABA vesicles since the B block is largely confined to layers parallel to the surface. The time evolution in Figure 7 reveals that microstructural formation occurs in successive, initially unconnected layers, where subsequent densification of the A block forms bridges between them.

The propagation of layers is reminiscent of morphologies obtained in homopolymer films during NIPS without a glassy dynamics and thermal fluctuations, whereby the propagation of layers is attributed to surface-directed spinodal decomposition.[41,42] Fluctuations are necessary for opening up pathways for N to diffuse into the film in homopolymer NIPS, otherwise a glassy skin would form on the surface. This phenomenon occasionally occurs in SNIPS below the isoporous surface, however, in most cases, N can diffuse through the domains formed by the A block since it is *not glassy*. This promotes lateral movement of N which cut off the formation of a continuous *glassy* polymer-rich domain, however allow the A block to densify, forming the aforementioned bridges.

We remark that morphologies generated by Blagojevic *et al.* do not exhibit the layer-like

structure we observe in our simulations.[30] We posit that the larger χ_{BN} values accessible to their simulation method inhibits the lateral diffusion of N, in turn precipitating vertically oriented polymer-rich domains that disrupts the formation of layers. It is also possible that the addition of thermal fluctuations may play a role in destabilizing the layer-like structure.

3.2.1 Nonsolvent selectivity

Up until now, we set $\chi_{AN} = 0.5$ and found significant structural rearrangement in the top selective layer of the membrane when $(\chi_{AS}, \chi_{BS}) = (1.2, 0.6)$ and $(\chi_{AS}, \chi_{BS}) = (1.1, 0.7)$. However, in our previous work we employed $\chi_{AN} = 1.0$ and found that morphologies in both 2D and 3D mostly retained the initial hexagonal packing in the selective layer following NIPS, even without glassy dynamics.[29] We investigate this further here, setting $\chi_{AN} = 1.0$ and performing simulations using the same pairs of (χ_{AS}, χ_{BS}) as in the previous section.

The time evolution and final morphologies are presented in Figure 8. We observe that, no matter the solvent selectivity, there is minimal structural rearrangement in the selective layer throughout the NIPS process; the hexagonally packed vertical cylinders do not collapse as they did when $\chi_{AN} = 0.5$. This is consistent with our previous work[29] and demonstrates the sensitivity of cylindrical orientation to the hydrophilicity of the minority block. The more hydrophilic the A block, the more swollen it becomes as N enters into the pores. The swelling of the A block not only promotes the expansion of the cylinders, increasing their diameter, but provides additional contact with the B block, allowing more N to enter and destabilize the entire surface structure. This is effect is clearly illustrated in Figure 7a where the expansion of the A block cylinders and destabilization of the B domain by N led to the bridging of two vertical cylinders, giving a nearly parallel cylinder.

We further observe that the surface-bulk connectivity is hampered by the increase in χ_{AN}. The connectivity produced by the least selective solvent seen in Figure 7 is lost when $\chi_{AN} = 1.0$ (Figure 8c). Snapshots at $t = 8\tau_R$ clearly show that the surface and bulk are initially connected, but soon those connections are pinched off. We hypothesize that as

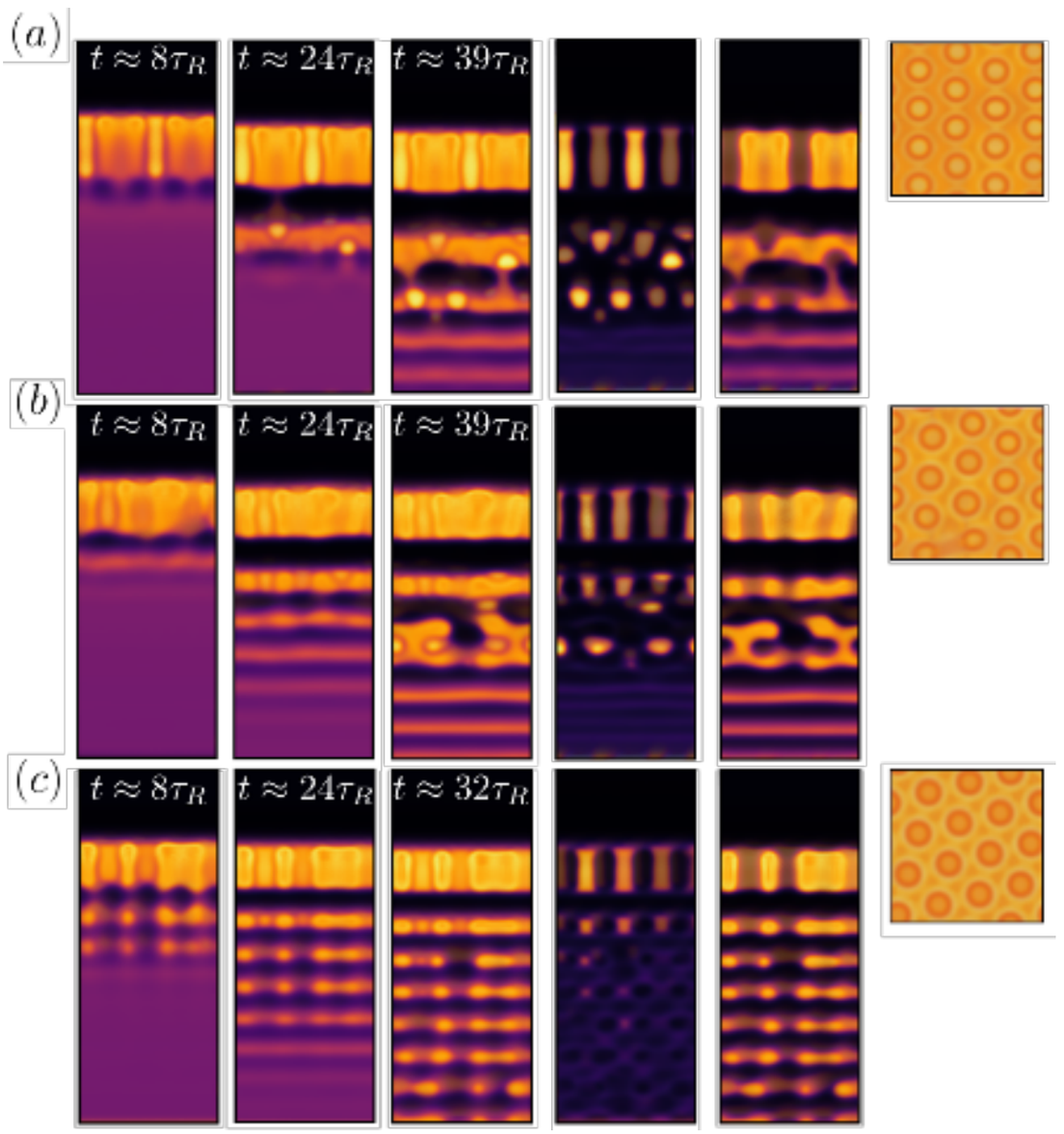

Figure 8: Time evolution of a morphology generated from a SNIPS simulation with $\chi_{AN} = 1.0$ and (a) $(\chi_{AS}, \chi_{BS}) = (1.2, 0.6)$, (b) $(\chi_{AS}, \chi_{BS}) = (1.1, 0.7)$ and (c) $(\chi_{AS}, \chi_{BS}) = (1.0, 0.8)$. The first five panels show a cross section of the film morphology and the last panel shows a top down view of the surface. The first three panels display $\phi_P(\mathbf{r}, t)$, the fourth displays $\phi_A(\mathbf{r}, t)$, the fifth panel displays the B block density $\phi_B(\mathbf{r}, t)$, and the last panel displays $\phi_P(\mathbf{r}, t)$. Snapshots of the total polymer density are labeled according to the Rouse time at which they were taken. Panels displaying the A and B block densities and the top down view of the surface correspond to the latest time shown in the time evolution.

more N enters the space between the surface and the first layer precipitated via NIPS, the tendrils extending from the surface recede backwards to avoid excessive contact with N. Furthermore, upon examining the A density profile for $(\chi_{AS}, \chi_{BS}) = (1.0, 0.8)$ in Figure 7, we can see an outward growth of A in forming the tendrils. The lack of swelling, however, hinders this growth which in turn hinders the continuous extension of the surface A and B domains. This growth, or generally, rearrangement, is necessary to provide a continuous transition from a microphase-separated structure in the surface to a macrophase-separated structure in the bulk.

The increase in χ_{AN} also impacts the bulk microstructure, notably enhancing the densification of A-rich domains. This is unsurprising as the A block not only wants to avoid contact with S, but also with N, leading to the population of A-rich pockets throughout the microstructure. Phase separation kinetics are also impeded by the large χ_{AN} leading to an overall slower phase separation of the film.

3.2.2 Concentration of nonsolvent in casting solution

In this section, we investigate how varying ϕ_N, the initial volume fraction of N in the film, impacts the morphology for each pair of (χ_{AS}, χ_{BS}) (Figure 6). Although, to the best of our knoweldge, no study investigating membrane formation via SNIPS has nonsolvent present in the initial film, studies employing dry/wet NIPS to fabricate membranes do often feature nonsolvent in the initial film.[54–56] Changing ϕ_N probes two different effects on our system: (1) varying the amount of N from the bath necessary to induce macrophase separation, and modifying phase separation time, and (2) changing the effective interaction between the solvent mixture and the A and B block, which we denote as χ_{AS}^{eff} and χ_{BS}^{eff}, respectively. Specifically, replacing S with N in the film decreases χ_{AS}^{eff} and increases χ_{BS}^{eff}, due to the opposite selectivity of S and N for the A and B blocks. Adding nonsolvent to the initial film has precedent in membrane fabrication

Figure 9 presents the simulation results for systems with $(\chi_{AS}, \chi_{BS}, \phi_N) = (1.2, 0.6, 0.1)$

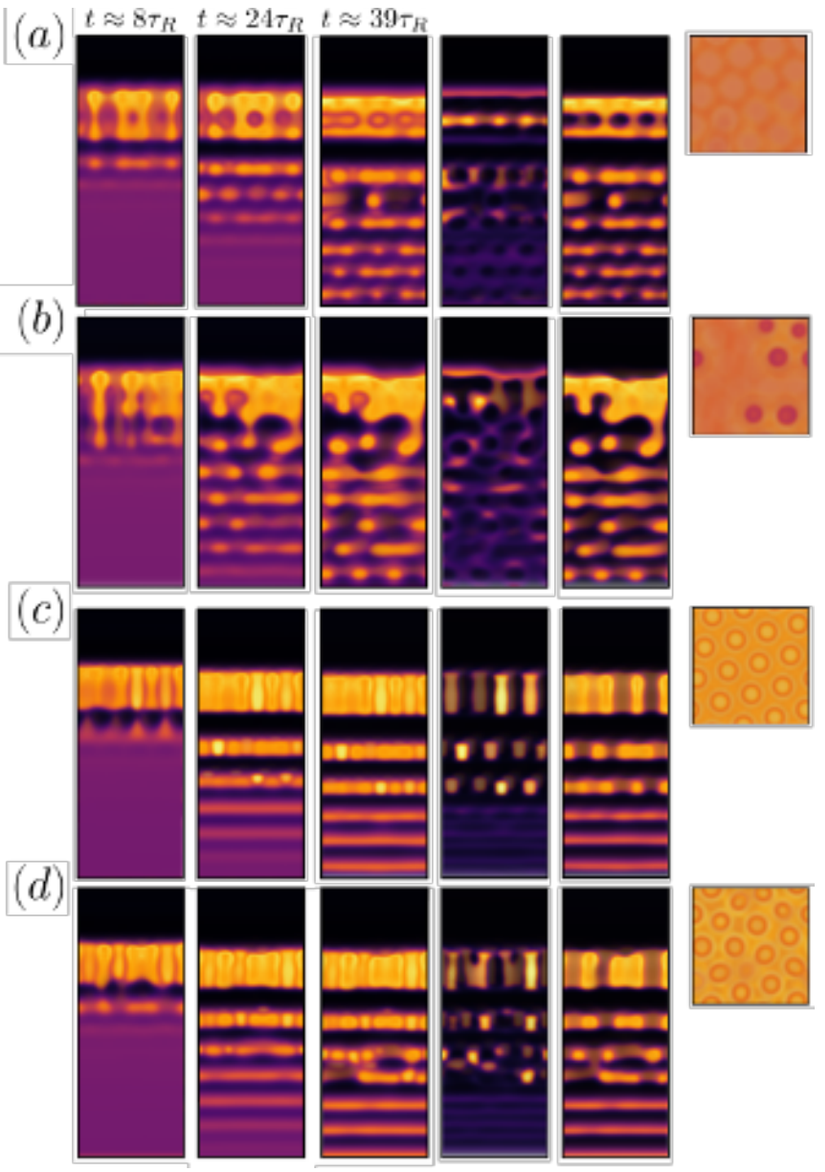

Figure 9: Time evolution of a morphology generated from a SNIPS simulation with (a, b) $\chi_{AN} = 0.5$ and (c, d) $\chi_{AN} = 1.0$. Other parameters used are (a, c) $(\chi_{AS}, \chi_{BS}, \phi_N) = (1.2, 0.6, 0.01)$, and (b, d) $(\chi_{AS}, \chi_{BS}, \phi_N) = (1.1, 0.7, 0.04)$. All morphologies have $\phi_P = 0.25$. The first five panels show a cross section of the film morphology and the last panel shows a top down view of the surface. The first three panels display $\phi_P(\mathbf{r}, t)$, the fourth displays $\phi_A(\mathbf{r}, t)$, the fifth panel displays the B block density $\phi_B(\mathbf{r}, t)$, and the last panel displays $\phi_P(\mathbf{r}, t)$. Snapshots of the total polymer density are labeled according to the Rouse time at which they were taken. Panels displaying the A and B block densities and the top down view of the surface correspond to the latest time shown in the time evolution.

and $(\chi_{AS}, \chi_{BS}, \phi_N) = (1.1, 0.7, 0.04)$. We performed simulations with these parameter sets for two values of χ_{AN}: $\chi_{AN} = 0.5$ and $\chi_{AN} = 1.0$. We see that increasing ϕ_N for each system further perturbs the initial surface ordering during NIPS. The most extreme case is seen in Figure 9a where $(\chi_{AS}, \chi_{BS}, \chi_{AN}, \phi_N) = (1.2, 0.6, 0.5, 0.01)$. All of the perpendicularly oriented cylinders collapse and combine to form a single sheet sandwiched between two B domains. This completely closes the pores on the surface, preventing the further exchange of N and S. It can also be seen when $(\chi_{AS}, \chi_{BS}, \chi_{AN}, \phi_N) = (1.1, 0.7, 1.0, 0.04)$, cylinders fuse together despite the larger value of χ_{AN}. We previously observed that decreasing χ_{AS} and increasing χ_{BS} stabilized the cylinders so it is difficult to attribute the structural rearrangement to the change in either χ^{eff}_{AS} or χ^{eff}_{BS}. However, we know generally that the diffusion of N into the surface perturbs the structure, thus replacing S with N in the casting solution should do the same. Furthermore, the replacement is uniform as opposed to N normally diffusing through the pores with minimal intrusion into the B domain. This introduces significant stress to the B domain, causing greater deformation in the surface structure than when no S was replaced.

Another observation is the gain in surface-bulk connectivity when $(\chi_{AS}, \chi_{BS}, \chi_{AN}, \phi_N) = (1.1, 0.7, 0.5, 0.04)$ (Figure 9b). This can be explained by both aforementioned effects of replacing S with N.

(1) By reducing the amount of additional N needed to initiate macrophase separation, less S leaves before we obtain a vitrified bulk microstructure, preventing the film from further receding. In turn, there is, over time, less force applied to the surface-bulk connecting tendrils antiparallel to the surface normal, allowing them to remain fixed.

(2) We argued previously that increasing χ_{BS} protects the tendrils from an influx of S that would solvate the B domain and pinch off the tendrils. Therefore, we expect that increasing χ^{eff}_{BS} contributes to the stability of the tendrils.

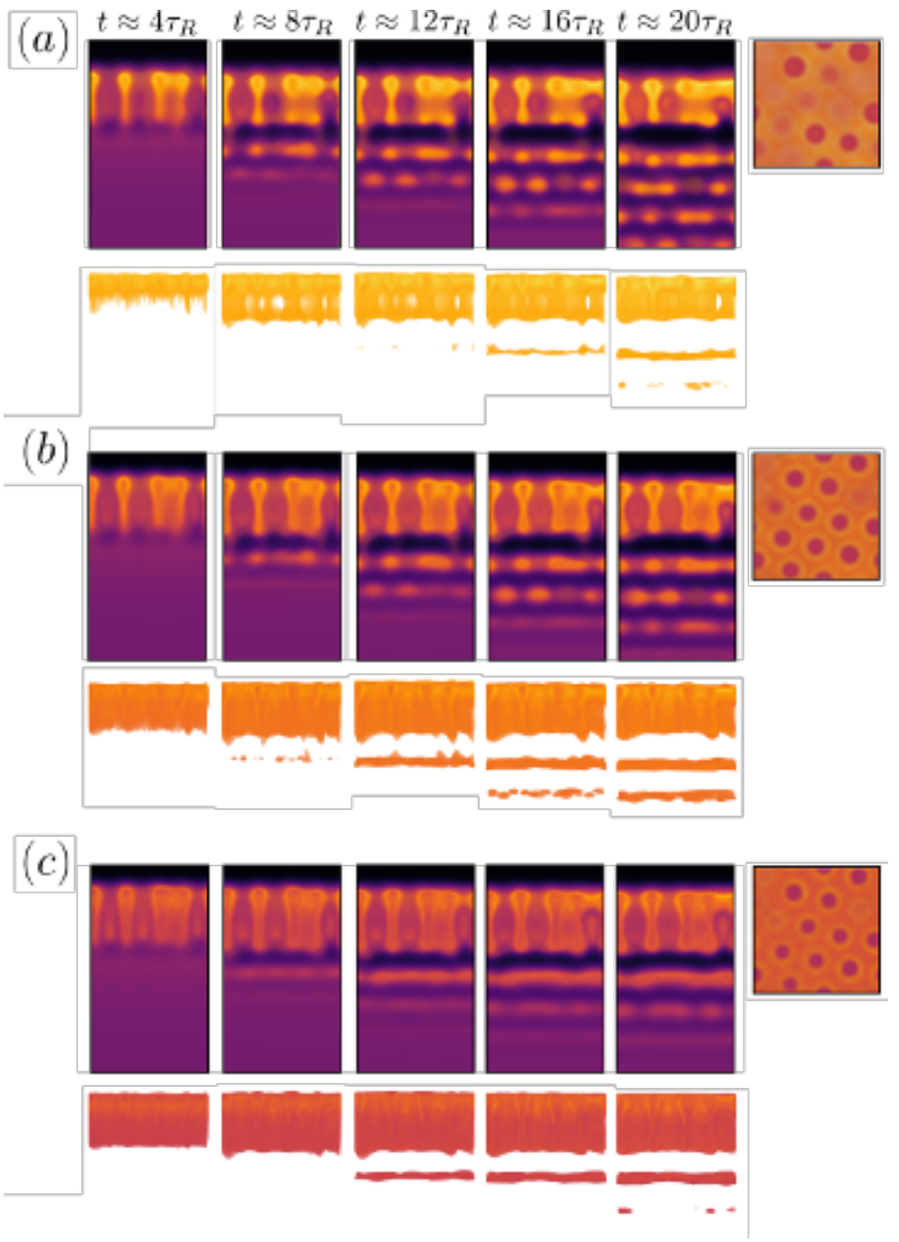

Figure 10: Time evolution of a morphology generated from a SNIPS simulation with $(\chi_{AS}, \chi_{BS}, \phi_N) = (1.1, 0.7, 0.01)$. The glass transition composition, ϕ_B^*, was varied with (a) $\phi_B^* = 0.6$, (b) $\phi_B^* = 0.5$, and (c) $\phi_B^* = 0.4$. The top rows display $\phi_P(\mathbf{r}, t)$ while the bottom rows display the glassy B block density, $\phi_B(\mathbf{r}, t) \geq \phi_B^*$. The last panels on each row show a top down view of the surface, displaying $\phi_P(\mathbf{r}, t)$. Snapshots are labeled according to the Rouse time at which they were taken.

3.2.3 Glass transition composition

Thus far, we have observed several sets of parameters that resulted in either a significant distortion to the surface hexagonal packing or a loss in surface-bulk connectivity, or both. We hypothesized a lower glass transition composition, ϕ_B^*, can prevent excessive surface deformation and help vitrify the surface-bulk connection before it can pinch off. Experimentally, it is possible to lower the glass transition temperature, and thus ϕ_B^*, by careful choice of solvent(s).[57]

Figure 10 presents the time evolution of $\phi_P(\mathbf{r}, t)$ and the glassy regions of the B block density, $\phi_B(\mathbf{r}, t) \geq \phi_B^*$. We applied three glass transition compositions, $\phi_B^* = [0.6, 0.5, 0.4]$, where all previous results employed $\phi_B^* = 0.6$. We can immediately see that a stricter glass transition prevents a significant loss of surface distortion; only a few pores close when $\phi_B^* \leq 0.5$. Interestingly, there appears to be no difference in the number of pores remaining reducing ϕ_B^* from 0.5 to 0.4. It is possible, that an even lower ϕ_B^* would prevent any pore from closing, however, we discuss below why this may not be preferable.

We found that lowering ϕ_B^* did not result in the full vitrification of a surface-bulk connection. A close look reveals that regions that became glassy in the channel between the surface and bulk had their B density sufficiently diluted such that $\phi_B(\mathbf{r}) < \phi_B^*$. This is clearly seen in Figure 10b where at time $t \approx 12\tau_R$ several glassy tendrils are protruding from the surface and bulk structures. By the time $t \approx 20\tau_R$, however, only a few glassy protrusions remain. To confirm the friction ratio $\gamma_B = 10^4$ is not too low, we also ran a simulation with $\gamma_B = 10^6$ and $(\chi_{AS}, \chi_{BS}, \phi_N, \phi_B^*) = (1.1, 0.7, 0.01, 0.5)$. The results in Figure SI2 demonstrate that a higher friction ratio does not sustain the glassy regions throughout the simulation time.

It would seem unlikely that choosing $\gamma_B = 10^6$, and hence reducing the mobility by 10^6, would allow unvitrification to occur over the time scale of the simulation, around 5×10^5 timesteps. However, the glass transition is implemented in the present work by modifying the mobility through a sigmoidal function with a width of 10^{-3}. Therefore, in regions where $\phi_B(\mathbf{r}) = 0.6$, the mobility is not decreased by a factor of 10^{-6} but instead 5×10^{-5}. It

is possible within the given time span that $\phi_B(\mathbf{r})$ decreases by half the sigmoidal width (5×10^{-2}) and thus escapes the glass regime.

We can see in Figure 10c that setting $\phi_B^* = 0.4$ actually reduces that amount of B that vitrifies in the surface-bulk channel. When $\phi_B^* = 0.5$ the glassy regions almost connect but when $\phi_B^* = 0.4$, the glassy regions barely protrude into the channel. We attribute this to a lack of mobility at the bottom of the surface layer due to excessive vitrification. As argued in section 3.2.1, forming a surface-bulk connection requires some structural rearrangement to transition from a microphase-separated structure to a macrophase-separated structure. Therefore, applying too low a glass transition composition will prevent sufficient rearrangement from occurring, inhibiting the formation of a surface-bulk connection.

Lowering ϕ_B^* generally prevents the bulk microstructure from coarsening completely. We observe in Figure 10c that employing $\phi_B^* = 0.4$ inhibits the formation of pores in the first bulk layer, impeding the diffusion of N further into the film. The addition of thermal fluctuations will aid in breaking up the glassy layer to form pores, analogous to how fluctuations are necessary in modeling homopolymer-based membrane formation since the surface does not have pores prior to NIPS.[42] We leave the addition of thermal fluctuations to future work.

3.2.4 Further investigations of surface-bulk connectivity

In previous sections we discussed how various parameters affect the surface-bulk connectivity. We briefly summarize our findings:

(1) Larger χ_{BS} favors surface-bulk connectivity.

(2) Increasing χ_{AN} inhibits connectivity.

(3) Lowering ϕ_B^* helps vitrify the surface-bulk connection but decreasing ϕ_B^* too much impedes connectivity.

(4) The bottom of the surface layer must have enough mobility to rearrange to form the connection with the bulk morphology.

In section 3.2.3 we found that surface-bulk connections that partially vitrified eventually

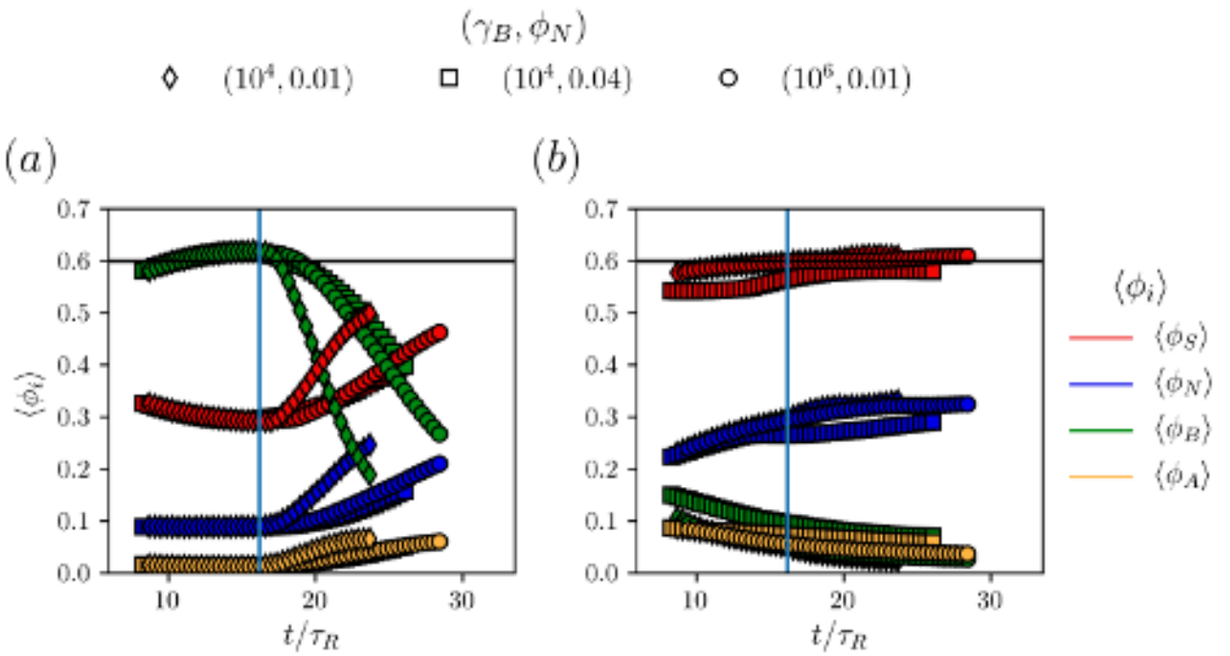

Figure 11: Time evolution of each spatially averaged species density $\langle\phi_i(\mathbf{r},t)\rangle$ over a region spanning $\Delta z \approx 1.4R_g$ space below the surface layer ending at $z \approx -3.96R_g$. In (a) we only average over densities which occupy grid points at which $\phi_B(\mathbf{r}, t \approx 16.2\tau_R) \geq \phi_B^*$, whereas in (b) this is done over all gridpoints within the $\Delta z \approx 1.4R_g$ space. We begin tracking at $t \approx 8.3\tau_R$ and finish tracking at $t \approx 26.1\tau_R$. We track species densities from three simulations with the parameter sets $(\gamma_B, \phi_N) = (10^4, 0.01)$ (diamonds), $(\gamma_B, \phi_N) = (10^4, 0.04)$ (squares), and $(\gamma_B, \phi_N) = (10^6, 0.01)$ (circles). All simulations used $(\chi_{AS}, \chi_{BS}) = (1.1, 0.7)$. Colors denote the species being averaged. A blue vertical line is plotted at $t \approx 16.2\tau_R$ indicating the time at which all grid points averaged over in (a) satisfied the condition $\phi_B(\mathbf{r}) \geq \phi_B^*$. A black horizontal line is plotted at $\langle\phi_i\rangle = 0.6$ to designate the glass transition composition, $\phi_B^* = 0.6$.

returned to a liquid state, thus allowing the connection to be pinched off. Our finding that large values of χ_{BS} enable surface-bulk connections to be formed suggest the flux of S might be interfering in the connection formation, but it remains unclear if the flux of S solvates already glassy B domains and destroys the partial connection. Furthermore, the role of N in the forming of a connection has yet to be investigated. In this section, we examine the trajectory of a partially vitrified connection by tracking each species density within the channel that the connection occupies.

In Figure 11a, we track the spatial average density of each species from time $t \approx 8.3\tau_R$ until $t \approx 26.1\tau_R$ over grid points that satisfy the condition $\phi_B(\mathbf{r}, t \approx 16.2\tau_R) \geq \phi_B^*$. From here on, we refer to these averages as $\langle\phi_i\rangle_{\text{glassy}}$ for each species i. In other words, at $t \approx 16.2\tau_R$ the grid points considered were occupied by a glassy B block. This is done within a $\Delta z \approx 1.4R_g$ thickness domain below the surface layer ending at $z \approx -3.96R_g$, which designates the channel in which the surface-bulk connection is constructed. Tracking the density at these grid points provides insight into how the connection vitrifies and eventually how it breaks apart. We perform this analysis for three parameter sets: $(\gamma_B, \phi_N) = (10^4, 0.01)$, $(\gamma_B, \phi_N) = (10^4, 0.04)$, and $(\gamma_B, \phi_N) = (10^6, 0.01)$, where for each we use $(\chi_{AS}, \chi_{BS}) = (1.1, 0.7)$. We saw that replacing S with N enabled a surface-bulk connection to be established, which is realized by increasing ϕ_N from 0.01 to 0.04 in the first two parameter sets. We also investigated the impact of γ_B, although increasing it did not significantly impact of a surface-bulk connection.

Examining $\langle\phi_B\rangle_{\text{glassy}}$ in Figure 11a, we see the gradual vitrification of the B block as it, on average, crosses and exceeds ϕ_B^*. Within this time, only $\langle\phi_S\rangle_{\text{glassy}}$ decreases, suggesting that the B block is filling the space left behind by S. At $t \approx 16.2\tau_R$, $\langle\phi_B\rangle_{\text{glassy}}$ peaks and begins to decrease for all parameter sets, indicating the un-vitrification of the B domain considered. By far the fastest rate of decrease is when $(\gamma_B, \phi_N) = (10^4, 0.01)$. In spite of increasing γ_B not enabling a sustained surface-bulk connection, we see evidence that it does slow down the breaking up of the B domain. We do not attempt to increase γ_B further for reasons of numerical stiffness. Interestingly, even when $(\gamma_B, \phi_N) = (10^4, 0.04)$, a system

which maintained one connection, we see the B domain slowly fall apart, although the rate is the slowest of the three systems.

The time at which $\langle\phi_B\rangle_{\text{glassy}}$ begins to decline marks the time at which the average of the other species begin to rise. We see $\langle\phi_S\rangle_{\text{glassy}}$ increases the fastest, followed by $\langle\phi_N\rangle_{\text{glassy}}$ for all three systems. We can see how this corresponds to the species densities averaged over the *entire channel*, i.e. not only over grid points satisfying $\phi_B(\mathbf{r}, t \approx 16.2\tau_R) \geq \phi_B^*$, in Figure 11b. We denote densities averaged over the entire channel as $\langle\phi_i\rangle_{\text{channel}}$. Over time, both $\langle\phi_S\rangle_{\text{channel}}$ and $\langle\phi_N\rangle_{\text{channel}}$ increase steadily; however we see $\langle\phi_N\rangle_{\text{channel}}$ increases slightly faster when $(\gamma_B, \phi_N) = (10^4, 0.01)$ and $(\gamma_B, \phi_N) = (10^6, 0.01)$. Accordingly, $\langle\phi_B\rangle_{\text{channel}}$ and $\langle\phi_A\rangle_{\text{channel}}$ monotonically decrease. These results indicate that any connection present at $t \approx 8.3\tau_R$ steadily deteriorate as more N and S enter the channel.

This suggests that the diffusion of S as it attempts to leave the film, and the diffusion of N as it enters the film, both damage the surface-bulk connections steadily. The time evolution of $\langle\phi_B\rangle_{\text{glassy}}$ shows that the vitrification process is slow, but once S and N start penetrating into those regions, a cascading effect of un-vitrification initiates, causing $\langle\phi_B\rangle$ in those regions to drop. Although we only look at grid points satisfying $\phi_B(\mathbf{r}, t \approx 16.2\tau_R) \geq \phi_B^*$, our observations apply to other sets of grid points which become completely glassy at all other times within the time span studied. This is evidenced by the fact that $\langle\phi_B\rangle_{\text{channel}}$ steadily decreases instead of sharply decreasing at any particular time.

Based on these observations, we can conclude that preserving surface-bulk connections amounts to preventing S and N from taking over the B domain. This can be done by increasing either χ_{BS} or χ_{BN}. This further explains why replacing S with N stabilized the connecting tendrils; the solvent mixture became more repulsive towards the B block, increasing χ_{BS}^{eff}. Our observations are also consistent with those made by Blagojevic *et al.*, where a large enough χ_{BN} was necessary to preserve the surface-bulk connectivity.[30] Mobility reduction has also shown to play a role — efforts to increase the B vitrification, e.g. by shifting the glass transition concentration or enhancing the friction ratio, should

support the durability of surface-bulk connections.

4. Summary and Conclusions

In this study we employed a workflow, developed in our previous work,[29] that models the SNIPS process to examine the effect of various parameters on the final morphology. The evaporation step was approximated using an equilibrium SCFT simulation where the resulting density profiles were then stitched onto a film-bath interface to produce an isoporous surface. DSCFT was then applied to simulate the mass exchange of solvent and nonsolvent, analogous to similar studies modeling homopolymer NIPS.[39–42] The block copolymer selected here is an AB diblock, where the A block is a hydrophilic minority block and the B block is hydrophobic majority block which also becomes glassy above a certain concentration. Our system has a single solvent S and a single nonsolvent N.

Many parameters were examined: solvent selectivity, initial film composition, nonsolvent selectivity, glass transition composition, etc. RPA was used to determine which parameter values led to a macrophase separated film, constraining the parameters used in this study. Larger values of χ_{AS} gave rise to ABA vesicles in 2D morphologies while smaller χ_{AS} led to morphologies mainly populated by AB spherical micelles. In both cases, the A block formed a corona that also bridged together multiple micelles to produce the membrane matrix. For ABA vesicles, however, the A block also fills an inner core which is swollen by N. A similar effect was seen in 3D, however the layered nature of the B domains makes it difficult to claim the structure is composed of connected micelles. We also found it was necessary to have a sufficiently large polymer concentration in the film to construct a fully connected membrane matrix.

Much of our investigation focused on two aspects of the membrane morphology that are crucial to its viability: (1) preserving the isoporous surface and (2) establishing a connection between the surface and bulk microstructure. Obtaining an isoporous surface is the primary

goal of employing block copolymer SNIPS over homopolymer NIPS, granting SNIPS membranes a superior performance.[12] Furthermore, without a stable surface-bulk connection, the surface will not have any mechanical support and thus detach after draining the nonsolvent. Therefore, it is crucial to identify parameters that preserve these two features. Below, we summarize the impact of each parameter on both features.

(1) We found that by minimizing $\chi_{AS} - \chi_{BS}$ we also minimize the distortion to the ordering in the surface layer. Increasing χ_{AN} had the largest impact in preserving the surface ordering, namely by preventing the A cylindrical cores from swelling and collapsing. Replacing S with N in the bulk of the film damages the surface ordering since more N is partitioned in the B domain, leading to significant surface rearrangement. As expected, lowering the glass transition composition, ϕ_B^*, prevents many pores from closing; however, beyond a certain limit lowering ϕ_B^* has no effect. We speculate that increasing χ_{BN} will have a stabilizing effect by preventing N from penetrating into the B domain.

(2) Increasing χ_{BS} helps stabilize the surface-bulk connection by preventing S from infiltrating connections and resolvating them. Larger values of χ_{AN} hamper rearrangement near the bottom of the surface layer that is necessary to transition from a microphase-separated morphology to a macrophase-separated morphology. Replacing S with N in the casting solution effectively increases χ_{BS} since $\chi_{BN} > \chi_{BS}$ and hence stabilizes the surface-bulk connection. A goldilocks zone is suggested to exist for ϕ_B^*: if too high, then the surface-bulk connection cannot vitrify and if too low, there is not enough chain mobility to form the connections in the first place. We also found that increasing χ_{BN} should help preserve the connection by sharpening the solution-B interface, averting the connections from pinching off.

These findings are expected to provide guidance for experimentalists seeking to fabricate membranes via SNIPS. Future work will look towards a more realistic model of the evaporation step to serve as input to the NIPS step simulated here. The addition of thermal fluctuations will also be an important step moving forward. A crucial improvement for fu-

ture work is employing larger and more realistic values of χ_{BN} for reasons discussed above. This work featured only a single solvent, although many experimental systems consist of more than one solvent.[14,17,19,20,46] We leave the incorporation of additional solvents to future work.

Supporting Information

The supporting information contains details on the adaptive time-stepper employed to avoid time-step errors due to negative densities. Furthermore, additional figures displaying an angled view of the A block, B block, and total polymer density for the pair of χ values: $\{(\chi_{AS}, \chi_{BS})\} = \{(1.0, 0.8), (1.1, 0.7), (1.2, 0.6)\}$ can be found. Finally, a figure presenting the time evolution of the simulation employing γ_B/γ_0 is included.

Acknowledgement

This work was supported as part of the Center for Materials for Water and Energy Systems (M-WET), an Energy Frontier Research Center funded by the U.S. Department of Energy, Office of Science, Basic Energy Sciences under Award #DE-SC0019272. The DSCFT methods utilized were developed under support from the NSF Condensed Matter and Materials Theory Program under DMR-2104255. Extensive use was made of the National Energy Research Scientific Computing Center (NERSC), a U.S. Department of Energy Office of Science User Facility located at Lawrence Berkeley National Laboratory, operated under Contract No. DE-AC02-05CH11231. Use was also made of computational facilities purchased with funds from the National Science Foundation (CNS-1725797) and administered by the Center for Scientific Computing (CSC). The CSC is supported by the California NanoSystems Institute and the Materials Research Science and Engineering Center (MRSEC; NSF DMR-2308708) at UC Santa Barbara.

References

(1) Tzanakakis, V. A.; Paranychianakis, N. V.; Angelakis, A. N. Water Supply and Water Scarcity. *Water* **2020**, *12*.

(2) Elimelech, M.; Phillip, W. A. The Future of Seawater Desalination: Energy, Technology, and the Environment. *Science* **2011**, *333*, 712–717.

(3) Goh, P. S.; Liang, Y. Y.; Ismail, A. F. Energy Efficient Seawater Desalination: Strategies and Opportunities. *Energy Technology* **2021**, *9*, 2100008.

(4) Puyol, D.; Batstone, D. J.; Hülsen, T.; Astals, S.; Peces, M.; Krömer, J. O. Resource Recovery from Wastewater by Biological Technologies: Opportunities, Challenges, and Prospects. *Frontiers in Microbiology* **2017**, *7*.

(5) Geise, G. M.; Lee, H.-S.; Miller, D. J.; Freeman, B. D.; McGrath, J. E.; Paul, D. R. Water purification by membranes: The role of polymer science. *Journal of Polymer Science Part B: Polymer Physics* **2010**, *48*, 1685–1718.

(6) Warsinger, D. M. et al. A review of polymeric membranes and processes for potable water reuse. *Progress in Polymer Science* **2018**, *81*, 209–237.

(7) *Membrane Technology and Applications*; John Wiley & Sons, Ltd, 2012.

(8) LOEB, S.; SOURIRAJAN, S. *Saline Water Conversion—II*; 1963; Chapter 9, pp 117–132.

(9) Guillen, G. R.; Pan, Y.; Li, M.; Hoek, E. M. V. Preparation and Characterization of Membranes Formed by Nonsolvent Induced Phase Separation: A Review. *Industrial & Engineering Chemistry Research* **2011**, *50*, 3798–3817.

(10) Werber, J. R.; Osuji, C. O.; Elimelech, M. Materials for next-generation desalination and water purification membranes. *Nature Reviews Materials* **2016**, *1*, 16018.

(11) Mochizuki, S.; Zydney, A. L. Theoretical analysis of pore size distribution effects on membrane transport. *Journal of Membrane Science* **1993**, *82*, 211–227.

(12) Zhang, Y.; Sargent, J. L.; Boudouris, B. W.; Phillip, W. A. Nanoporous membranes generated from self-assembled block polymer precursors: Quo Vadis? *Journal of Applied Polymer Science* **2015**, *132*.

(13) Hampu, N.; Werber, J. R.; Chan, W. Y.; Feinberg, E. C.; Hillmyer, M. A. Next-Generation Ultrafiltration Membranes Enabled by Block Polymers. *ACS Nano* **2020**, *14*, 16446–16471, PMID: 33315381.

(14) Abetz, V. Isoporous Block Copolymer Membranes. *Macromolecular Rapid Communications* **2015**, *36*, 10–22.

(15) Nunes, S. P. Block Copolymer Membranes for Aqueous Solution Applications. *Macromolecules* **2016**, *49*, 2905–2916.

(16) Nunes, S. P. In *Sustainable Nanoscale Engineering*; Szekely, G., Livingston, A., Eds.; Elsevier, 2020; pp 297–316.

(17) Peinemann, K.-V.; Abetz, V.; Simon, P. F. W. Asymmetric superstructure formed in a block copolymer via phase separation. *Nature Materials* **2007**, *6*, 992–996.

(18) Müller, M.; Abetz, V. Nonequilibrium Processes in Polymer Membrane Formation: Theory and Experiment. *Chemical Reviews* **2021**, *121*, 14189–14231, PMID: 34032399.

(19) Stegelmeier, C.; Filiz, V.; Abetz, V.; Perlich, J.; Fery, A.; Ruckdeschel, P.; Rosenfeldt, S.; Förster, S. Topological Paths and Transient Morphologies during Formation of Mesoporous Block Copolymer Membranes. *Macromolecules* **2014**, *47*, 5566–5577.

(20) Marques, D. S.; Dorin, R. M.; Wiesner, U.; Smilgies, D.-M.; Behzad, A. R.; Vainio, U.; Peinemann, K.-V.; Nunes, S. P. Time-resolved GISAXS and cryo-microscopy character-

ization of block copolymer membrane formation. *Polymer* **2014**, *55*, 1327–1332, Special Issue of Polymer Membranes.

(21) Hu, M.; Li, X.; Heller, W. T.; Bras, W.; Rzayev, J.; Russell, T. P. Using Grazing-Incidence Small-Angle Neutron Scattering to Study the Orientation of Block Copolymer Morphologies in Thin Films. *Macromolecules* **2023**, *56*, 2418–2428.

(22) Sutisna, B.; Polymeropoulos, G.; Musteata, V.; Peinemann, K.-V.; Avgeropoulos, A.; Smilgies, D.-M.; Hadjichristidis, N.; Nunes, S. P. Design of block copolymer membranes using segregation strength trend lines. *Mol. Syst. Des. Eng.* **2016**, *1*, 278–289.

(23) Tsige, M.; Mattsson, T. R.; Grest, G. S. Morphology of Evaporated Multiblock Copolymer Membranes Studied by Molecular Dynamics Simulations. *Macromolecules* **2004**, *37*, 9132–9138.

(24) Paradiso, S. P.; Delaney, K. T.; García-Cervera, C. J.; Ceniceros, H. D.; Fredrickson, G. H. Block Copolymer Self Assembly during Rapid Solvent Evaporation: Insights into Cylinder Growth and Stability. *ACS Macro Letters* **2014**, *3*, 16–20, PMID: 35632862.

(25) Berezkin, A. V.; Papadakis, C. M.; Potemkin, I. I. Vertical Domain Orientation in Cylinder-Forming Diblock Copolymer Films upon Solvent Vapor Annealing. *Macromolecules* **2016**, *49*, 415–424.

(26) Hao, J.; Wang, Z.; Wang, Z.; Yin, Y.; Jiang, R.; Li, B.; Wang, Q. Self-Assembly in Block Copolymer Thin Films upon Solvent Evaporation: A Simulation Study. *Macromolecules* **2017**, *50*, 4384–4396.

(27) Dreyer, O.; Ibbeken, G.; Schneider, L.; Blagojevic, N.; Radjabian, M.; Abetz, V.; Müller, M. Simulation of Solvent Evaporation from a Diblock Copolymer Film: Orientation of the Cylindrical Mesophase. *Macromolecules* **2022**, *55*, 7564–7582.

(28) Blagojevic, N.; Müller, M. Multiscale Modeling of Grain-Boundary Motion in Cylinder-Forming Block Copolymers. *ACS Polymers Au* **2023**, *3*, 96–117.

(29) Grzetic, D. J.; Cooper, A. J.; Delaney, K. T.; Fredrickson, G. H. Modeling Microstructure Formation in Block Copolymer Membranes Using Dynamical Self-Consistent Field Theory. *ACS Macro Letters* **2023**, *12*, 8–13, PMID: 36521059.

(30) Blagojevic, N.; Müller, M. Simulation of Membrane Fabrication via Solvent Evaporation and Nonsolvent-Induced Phase Separation. *ACS Applied Materials & Interfaces* **2023**, *15*, 57913–57927, PMID: 37222486.

(31) Fredrickson, G., et al. *The equilibrium theory of inhomogeneous polymers*; Oxford University Press on Demand, 2006.

(32) Helfand, E. Theory of inhomogeneous polymers: Fundamentals of the Gaussian random-walk model. *The Journal of Chemical Physics* **1975**, *62*, 999–1005.

(33) Düchs, D.; Delaney, K. T.; Fredrickson, G. H. A multi-species exchange model for fully fluctuating polymer field theory simulations. *The Journal of Chemical Physics* **2014**, *141*, 174103.

(34) Fraaije, J. G. E. M. Dynamic density functional theory for microphase separation kinetics of block copolymer melts. *J. Chem. Phys.* **1993**, *99*, 9202.

(35) van Vlimmeren, B. A. C.; Fraaije, J. G. E. M. Calculation of noise distribution in mesoscopic dynamics models for phase separation of multicomponent complex fluids. *Comput. Phys. Commun.* **1996**, *99*, 21–28.

(36) Hasegawa, R.; Doi, M. Adsorption Dynamics. Extension of Self-Consistent Field Theory to Dynamical Problems. *Macromolecules* **1997**, *30*, 3086–3089.

(37) Müller, M.; Schmid, F. Incorporating fluctuations and dynamics in self-consistent field

theories for polymer blends. *Advanced Computer Simulation Approaches for Soft Matter Sciences II* **2005**, 1–58.

(38) Yeung, C.; Shi, A.-C. Formation of Interfaces in Incompatible Polymer Blends: A Dynamical Mean Field Study. *Macromolecules* **1999**, *32*, 3637–3642.

(39) Tree, D. R.; Delaney, K. T.; Ceniceros, H. D.; Iwama, T.; Fredrickson, G. H. A multi-fluid model for microstructure formation in polymer membranes. *Soft Matter* **2017**, *13*, 3013–3030.

(40) Tree, D. R.; Iwama, T.; Delaney, K. T.; Lee, J.; Fredrickson, G. H. Marangoni Flows during Nonsolvent Induced Phase Separation. *ACS Macro Letters* **2018**, *7*, 582–586, PMID: 35632935.

(41) Tree, D. R.; F. Dos Santos, L.; Wilson, C. B.; Scott, T. R.; Garcia, J. U.; Fredrickson, G. H. Mass-transfer driven spinodal decomposition in a ternary polymer solution. *Soft Matter* **2019**, *15*, 4614–4628.

(42) Garcia, J. U.; Iwama, T.; Chan, E. Y.; Tree, D. R.; Delaney, K. T.; Fredrickson, G. H. Mechanisms of Asymmetric Membrane Formation in Nonsolvent-Induced Phase Separation. *ACS Macro Letters* **2020**, *9*, 1617–1624, PMID: 35617063.

(43) Villet, M. C.; Fredrickson, G. H. Efficient field-theoretic simulation of polymer solutions. *J. Chem. Phys.* **2014**, *141*.

(44) Vigil, D. L.; Delaney, K. T.; Fredrickson, G. H. Quantitative Comparison of Field-Update Algorithms for Polymer SCFT and FTS. *Macromolecules* **2021**, *54*, 9804–9814.

(45) Ceniceros, H. D.; Fredrickson, G. H. Numerical Solution of Polymer Self-Consistent Field Theory. *Multiscale Model. Simul.* **2004**, *2*, 452–474.

(46) Marques, D. S.; Vainio, U.; Chaparro, N. M.; Calo, V. M.; Bezahd, A. R.; Pitera, J. W.;

Peinemann, K.-V.; Nunes, S. P. Self-assembly in casting solutions of block copolymer membranes. *Soft Matter* **2013**, *9*, 5557–5564.

(47) Blanazs, A.; Armes, S. P.; Ryan, A. J. Self-Assembled Block Copolymer Aggregates: From Micelles to Vesicles and their Biological Applications. *Macromolecular Rapid Communications* **2009**, *30*, 267–277.

(48) Mai, Y.; Eisenberg, A. Self-assembly of block copolymers. *Chem. Soc. Rev.* **2012**, *41*, 5969–5985.

(49) Shen, H.; Eisenberg, A. Morphological Phase Diagram for a Ternary System of Block Copolymer PS310-b-PAA52/Dioxane/H2O. *The Journal of Physical Chemistry B* **1999**, *103*, 9473–9487.

(50) Lim Soo, P.; Eisenberg, A. Preparation of block copolymer vesicles in solution. *Journal of Polymer Science Part B: Polymer Physics* **2004**, *42*, 923–938.

(51) Hansen, C. M. *Hansen solubility parameters: a user's handbook*; CRC press, 2007.

(52) Hibi, Y.; Hesse, S. A.; Yu, F.; Thedford, R. P.; Wiesner, U. Structural Evolution of Ternary Amphiphilic Block Copolymer Solvent Systems for Phase Inversion Membrane Formation. *Macromolecules* **2020**, *53*, 4889–4900.

(53) Stropnik, Č.; Musil, V.; Brumen, M. Polymeric membrane formation by wet-phase separation; turbidity and shrinkage phenomena as evidence for the elementary processes. *Polymer* **2000**, *41*, 9227–9237.

(54) Pesek, S.; Koros, W. Aqueous quenched asymmetric polysulfone membranes prepared by dry/wet phase separation. *Journal of Membrane Science* **1993**, *81*, 71–88.

(55) Bridge, A. T.; Pedretti, B. J.; Brennecke, J. F.; Freeman, B. D. Preparation of defect-free asymmetric gas separation membranes with dihydrolevoglucosenone (CyreneTM) as a greener polar aprotic solvent. *Journal of Membrane Science* **2022**, *644*, 120173.

(56) Bridge, A. T.; Wamble, N. P.; Santoso, M. S.; Brennecke, J. F.; Freeman, B. D. Defect-free asymmetric Matrimid® gas separation membranes using dihydrolevoglucosenone (Cyrene™) as a greener polar aprotic solvent than traditional solvents. *Journal of Membrane Science* **2024**, *691*, 122221.

(57) Yoshioka, A.; Tashiro, K. Solvent Effect on the Glass Transition Temperature of Syndiotactic Polystyrene Viewed from Time-Resolved Measurements of Infrared Spectra at the Various Temperatures and Its Simulation by Molecular Dynamics Calculation. *Macromolecules* **2004**, *37*, 467–472.